

Charged-particle evaporation and pre-equilibrium emission in 1.2 GeV proton-induced spallation reactions

C.-M. Herbach^{a,*}, D. Hilscher^a, U. Jahnke^a, V.G. Tishchenko^{a,1},
J. Galin^b, A. Letourneau^{b,2}, A. Péghaire^b, D. Filges^c, F. Goldenbaum^c,
L. Pienkowski^d, W.U. Schröder^e, J. Töke^e

^a *Hahn-Meitner-Institut Berlin, Glienickerstr. 100, D-14109 Berlin, Germany*

^b *GANIL (IN2P3-CNRS, DSM-CEA) BP 5027, F-14076 Caen, Cedex 05, France*

^c *Forschungszentrum Jülich, Institut für Kernphysik, D-52428 Jülich, Germany*

^d *Heavy Ion Laboratory, Warsaw University, 02-093 Warszawa, Poland*

^e *University of Rochester, NY 14627, USA*

Received 31 May 2005; received in revised form 13 September 2005; accepted 26 October 2005

Available online 21 November 2005

Abstract

Absolute cross sections, energy spectra, and angular distributions have been measured for ${}^{1,2,3}\text{H}$, ${}^{3,4,6}\text{He}$, ${}^{6,7,8,9}\text{Li}$ and ${}^{7,9,10}\text{Be}$ isotopes produced in 1.2 GeV proton-induced spallation reactions with targets between Al and Th. Results of simulation calculations with the intra-nuclear cascade code INCL2.0 coupled to the statistical model GEMINI are in good agreement with these data, as to charged-particle evaporation, mean excitation energy, and mean linear momentum transfer. The pre-equilibrium emission of composite particles, not accounted for in these simulations, however, typically contributes to the total production of composite particles by 40–60% for ${}^2\text{H}$ and ${}^3\text{He}$, 20–40% for ${}^3\text{H}$, 5–20% for ${}^4\text{He}$, and about 15–25% for Li and Be. The composite pre-equilibrium particles together carry off a mean energy of up to 50 MeV, i.e., about 30% compared to the mean energy released by particle evaporation. For deuterons, pre-equilibrium emission is shown to be well described by surface coalescence while definitely other mechanisms are required for ${}^4\text{He}$ and heavier clusters.

© 2005 Elsevier B.V. All rights reserved.

PACS: 25.40.-h; 25.40.Sc; 24.10.Lx; 24.10.Pa; 29.30.Ep; 29.40.Wk

* Corresponding author. Tel.: +49 30 8062 2717; fax: +49 30 8062 2523.

E-mail address: herbach@hmi.de (C.-M. Herbach).

¹ Present address: Joint Institute for Nuclear Research, 141980 Dubna, Russia.

² Present address: DAPNIA/SPhN, CEA/Saclay, F-91191 Gif-sur-Yvette, France.

Keywords: NUCLEAR REACTIONS Al, Ti, Fe, Ni, Cu, Zr, Ag, Ho, Ta, W, Au, Pb, Th(p, X), $E = 1.2$ GeV; measured light charged particles isotopic production σ , $\sigma(E, \theta)$; deduced role of pre-equilibrium emission. Intra-nuclear cascade and statistical evaporation model analysis

1. Introduction

Medium-energy proton-induced spallation reactions present significant interest for a wide range of applications and fundamental research fields. They are at the crux of spallation neutron sources [1], transmutation of nuclear waste in accelerator driven systems [2], cosmology and astrophysics [3], cosmic ray physics [4,5], planetary and geochemical science [6], and, last but not least, nuclear physics. These considerations have motivated the NESSI Collaboration to investigate systematically spallation reactions induced by protons of 0.8–2.5 GeV incident energy [7–13]. The motivation for this programme is, in fact, twofold. First, the applications mentioned above call for an experimental validation of available spallation reaction models, before costly and ambitious engineering endeavours can rely on simulations and extrapolations based on such models. For instance, structural materials of the target station of a spallation neutron source are exposed to intense GeV proton beams and must thus withstand the internal production and retention of large amounts of hydrogen and helium. Since the amounts of the latter gas are of critical significance to the life span of a target station, reliable production estimates are needed for design and engineering processes. Second, spallation reactions are interesting to fundamental nuclear physics because proton- as well as antiproton-induced reactions produce nuclei at high thermal excitation energies [14,15] but with presumably little compression, deformations, or spins. These characteristics allow one to study the decay of relatively well defined, thermally high excited nuclei, e.g., nuclear fission at high excitation energies [16,17]. To illustrate the above opportunity, thermal excitation energies of up to about 600 MeV [13] and 800 MeV [12] can be obtained in spallation reactions with Au by protons of 1.2 GeV and 2.5 GeV kinetic energy, respectively. This latter excitation is only 100–200 MeV lower than generated in reactions with the more exotic beam of 1.2 GeV antiprotons [14].

The first objective of the present work concerns the measurement of total cross sections for hydrogen and helium isotopes produced in 1.2 GeV proton-induced reactions. Previous measurements of such cross sections have employed essentially three methods: (i) volumetric gas measurements combined with mass spectrometry [18–27] and, in the case of tritium, with activation methods, (ii) measurements using detector telescopes or time-of-flight methods [9,12, 28–33], and (iii) projectile fragmentation in reactions with inverse kinematics, employing magnetic spectrometers [34–36]. To some extent, these methods complement one another. For example, experiments with detector telescopes provide also particle energy spectra, which are useful to distinguish between evaporative and pre-equilibrium particle emission, while volumetric gas measurements are not influenced by any energy threshold.

Only few experimental results have been previously available in the investigated proton energy range at about 1.2 GeV although this energy is of particular importance for applications [1]. Moreover, systematic deviations between results obtained with methods (i) and (ii) have been reported in Ref. [9] for targets in the iron–nickel region, while for lead targets the results of the two methods seem to agree reasonably well as pointed out in Ref. [27]. To resolve existing discrepancies, the present work has remeasured the production cross sections for $E_p = 1.2$ GeV. Furthermore, the number of investigated reactions has been extended to all together 13 target nuclei ranging from Al up to Th.

The second objective of the present study is to determine the isotopic ratios for evaporation (EV) and pre-equilibrium (PE) particle emission. According to current views, spallation reactions are often seen as three-step reactions. The first step is best illustrated by an intra-nuclear cascade (INC) of successive nucleon–nucleon collisions. During this stage, a large fraction of the initial kinetic energy of the projectile is carried off by energetic cascade nucleons and pions which succeed to escape from the target. On the other hand, depending on the impact parameter, a larger or smaller number of involved nucleons remains in the residual nucleus, carrying the dissipated excitation energy. In a second reaction step, almost concurrently with the INC and prior to the attainment of statistical equilibrium, besides highly energetic nucleons also composite particles are emitted. Subsequently, at the third reaction step, the equilibrated residual nucleus deexcites via particle evaporation. The first and the last reaction steps are well established in the framework of various models. The intermediate step, however, the stage at which pre-equilibrium emission of nucleons and composite particles takes place, is not yet well understood, and various theoretical attempts have been made to solve this open question.

At least in a certain sense, pre-equilibrium emission of nucleons is inherently considered by the intra-nuclear cascade. The kinetic energy spectra predicted for cascade neutrons and protons extend from the high-energy part down to the low energies of the evaporation region. The basic assumption of the INC approach, namely the interaction between quasi-free nucleons, becomes, however, questionably at such low energies. This is the reason why various simulation codes (e.g., CEM [37,38], LAHET [39,40], FLUKA [41]) consider a separate pre-equilibrium phase which follows the INC before evaporation. Most frequently semi-classical exciton models based on the ideas of Griffin [42] and Blann [43] are employed, envisioning the equilibrating system to pass through configurations of single-particle excitations (“particles” and “holes”), starting from initial conditions as adopted from the final INC stage. The occurrence of configurations capable of particle emission, i.e., with “particles” at levels high enough to escape the nucleus, is estimated in a statistical manner. As to the energy spectra of neutrons and protons, reasonable agreement has been noticed in comparison between experiment and simulation calculations. However, the original concept of the exciton model fails to reproduce the strongly forward peaked angular distribution, and the theories of complex particle emission are still deficient [44]. The emission of light clusters in exciton models is usually described either by the hypothesis of pre-formed particles (treated as special excitons) [45], or by a coalescence assumption, that allows the excitons to condense with a certain probability if their location in phase space is close enough to each other [46,47]. A semi-empirical parametrisation used in the calculations of Mashnik et al. [38] provides a reasonable fit of the experimental data obtained for ^3He and ^4He in the reactions $p + \text{Ag}$ at 300 and 480 MeV [48].

A large number of alternative models have also been proposed. The emission of energetic particles from excited local zones of chemical equilibrium (“fireball” or “firestreaks”) have been discussed for heavy-ion reactions [49,50] as well as for proton-induced reactions [51,52]. Further pre-equilibrium models correlate the emission of fast composite particles directly to the motion of the cascade nucleons as calculated by the INC. This idea is in particular motivated by the forward peaked angular distribution of highly energetic composite particles which is similar to those of protons and neutrons. One of the applied concepts deals with pre-formed particles—mainly located close to the nucleus surface—which are released by energetic cascade nucleons in “pick-up” or “knock-out” interactions [44]. Another concept [53,54] assumes the complex particles to be generated through successive elementary reactions as $p + n \rightarrow d + \pi^0$, $d + p \rightarrow ^3\text{He} + \pi^0$, etc.

The observation that the momentum distribution of light composite particles as measured at different angles can be traced back by a simple power law to the corresponding proton distri-

butions [55] suggests to apply a coalescence approach to model the pre-equilibrium composite particle production. Although the number of cascade nucleons in proton-induced reactions is quite small, some implementations indeed restrict the coalescence to cascade nucleons [38,56] as originally proposed by Buttler et al. [57]. However, it has been early considered to accept also other nucleons from the Fermi sea, at least from the tail of the momentum distribution, to contribute to the cluster formation [58]. Following this idea, two very similar implementations have been recently developed to describe the composite particle emission in nucleon-induced spallation reactions by surface coalescence or percolation models [12,59]. These models allow emission of clusters *at any time* during the cascade stage.

The work of Letourneau et al. [12] presents a detailed analysis of the reaction $p(2.5 \text{ GeV}) + \text{Au}$. While the parameters of the coalescence model have been chosen to fit the kinetic energy spectra measured at the forward angle of 30° , the simulation calculations were able to reproduce the energy spectra of deuterons, tritons and ^3He with the same parameters at backward angles, and also for selected data corresponding to different bins of the thermal remnant excitation energy. On the other hand, with physically appropriate phase space parameters it was impossible to achieve a similar agreement with the measured ^4He spectra. A further deficiency of the calculations noticed in Ref. [12] was that the experimental proton data are significantly underestimated by the calculations between 40 and 150 MeV after introduction of coalescence while they were rather satisfactorily accounted for in the absence of coalescence. Similar results have been reported by Boudard et al. [59] for the comparison of the simulation calculations with the experimental data of the reactions $p + \text{Au}$ at 2.5 GeV and $n + \text{Cu}$ and Bi at 542 MeV, taken from [12] and [60], respectively.

An even more sophisticated microscopical approach to model complex particle emission from the early stage of proton-induced reactions on Al and Fe has been presented by Chiba et al. [61]. The cascade model was replaced by a Quantum Molecular Dynamics (QMD) model which inherently includes the emission of light composite particles. The application of QMD to heavy target nuclei is complicated and very computer time consuming. However, first results have been recently published by Fan et al. [62,63] for proton-induced reactions with Nb, Au, and Pb.

It is the aim of the present investigation to provide a comprehensive data set for sensitive benchmark tests of new theoretical approaches to describe the pre-equilibrium particle emission. The present work investigates systematically evaporative equilibrium and pre-equilibrium emission of p , d , t , ^3He , and ^4He , including particle energy spectra up to at least 100 MeV. Furthermore, the emission of the more complex fragments ^6He , $^{6,7,8,9}\text{Li}$, and $^{7,9,10}\text{Be}$ have been experimentally studied. All these investigations were performed for target nuclei between Al and Th, and with incident protons of 1.2 GeV energy.

Experimental results are systematically compared with the predictions of the intra-nuclear cascade code INCL2.0 [64] modelling the prompt emission of highly energetic, i.e., pre-equilibrium, nucleons while PE model calculations of composite particles are not considered. The output event data of the INCL2.0 Monte Carlo code for the intermediate target-like remnant, consisting of remnant mass and atomic numbers, its excitation energy and linear momentum, are then used as input to the statistical model code GEMINI [65]. This code calculates the statistical decay of the excited target remnant via evaporation of neutrons, light charged particles (LCPs) and intermediate-mass fragments (IMFs). Standard parameters have been used and no attempt has been made to optimise the parameters. In the INCL2.0 code, the depth of the potential well was set to $V_0 = 45 \text{ MeV}$. The reaction yields are normalised to the inelastic reaction cross sections as evaluated in the systematics from Ref. [66]. In the GEMINI code (version 5/97), the level density parameter was set to $a = A/10 \text{ MeV}^{-1}$, $a_f/a_n = 1.0$, and symmetric fission was accounted

for. The transmission coefficients were calculated according to the incoming wave boundary condition (IWBC option). Particle evaporation has been treated by Hauser–Feshbach formalism for neutrons and charged particles (including some unstable isotopes and excited states) up to $Z = 4$.

In some cases, additional comparisons are also presented with the results of simulation calculations using the Los Alamos High Energy Transport code LAHET [39] in the version 2.7d as well as a new upgrade of the Liège intra-nuclear cascade model INCL4.2 [67] coupled to the evaporation–fission model of Schmidt [68,69] in the version KHSv3p. For the simulation calculations with LAHET, a Bertini-type INC model [70] was available for 1.2 GeV incident proton energy. PE-emission exploiting an exciton model [40] was accounted for in the performed calculations. Two different descriptions of the statistical evaporation formalism have been employed in LAHET: (i) the Dresner-like [71] evaporation model ORNL, and (ii) the RAL evaporation–fission model [72] with excitation-energy dependent Coulomb barriers [73]. For the description of the level density distribution, the Gilbert–Cameron–Cook–Ignatyuk [74] formalism has been applied.

The codes INCL4.2 and KHSv3p have been used with the same parameters as given in [67], i.e., with the potential depth of $V_0 = 45$ MeV and the scaling factor $f_{\text{stop}} = 1$ which controls the stopping time of the INC process.

The following Section 2 describes the experiment, with special emphasis on the corrections applied in the determination of absolute cross sections and the associated uncertainties. In Section 3, experimental results are presented for total production cross sections, which are compared with both, previous measurements and model calculations. Measured energy spectra and angular distributions are analysed to distinguish between contributions from evaporation and pre-equilibrium emission. The energy carried-off by PE composite particles is compared with the mean thermal excitation energy deposited in the residual nucleus after the intra-nuclear cascade which has been determined from the measured multiplicities of evaporative neutrons and LCPs. The linear momentum transfer from the projectile to the target nucleus is deduced from the angular distribution of evaporated ^4He . Finally, Section 4 presents a summary and conclusions.

2. Experimental method and data analysis

The measurements discussed in this paper have been performed with the external proton beam from the Cooler Synchrotron Facility COSY of the Forschungszentrum Jülich. The experiments utilised the 4π -detector NESSI (NEutron Scintillator tank and SIlicon ball) for an efficient and simultaneous detection of neutrons and charged particles. In addition to the Berlin Neutron Ball (BNB), and the Berlin Silicon Ball (BSiB), the setup has been equipped with six ancillary four-element detector-telescopes and a set of plastic scintillation detectors for beam diagnostics purposes. A schematic drawing of the experiment is shown in Fig. 1. Detailed descriptions of the NESSI detector are given elsewhere [75,76]. In the following, those parts of the detector are described again briefly that are of special importance for the measurement and the uncertainties of the absolute production cross sections of light charged particles and intermediate-mass fragments.

2.1. Detectors

The outer spherical vessel of the NESSI detector contains the scintillator liquid of the Berlin Neutron Ball. BNB provides a fast signal which indicates the occurrence of a reaction with a low inelasticity threshold of about 2 MeV. Furthermore, the multiplicity of emitted neutrons is

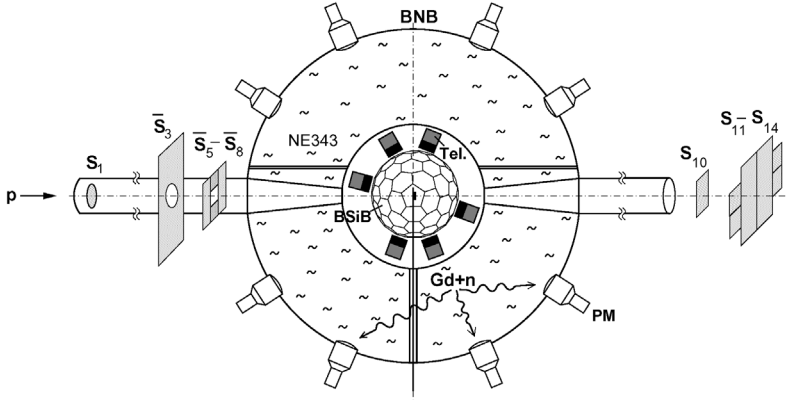


Fig. 1. Experimental setup of the NESSI detector installed at the COSY beam line (from Ref. [76]). The two 4π -detectors BNB for neutrons and BSiB for charged particles are supplemented by six fourfold detector telescopes. A thin plastic scintillator S_1 is used to count the incident beam protons and to deliver start signals for time-of-flight measurements. Further scintillation detectors are exploited as active beam collimators \bar{S}_3 – \bar{S}_8 and for beam diagnostics S_{10} – S_{14} .

measured with high efficiency for evaporated and low efficiency for highly energetic neutrons. The inner vacuum chamber of the BNB houses the Berlin Silicon Ball (BSiB) consisting of 151, 500- μm thick, silicon detectors with four different shapes: regular pentagons, regular hexagons, and two different shaped irregular hexagons. The solid angles covered by the individual BSiB detectors have been determined experimentally to (66.9 ± 0.8) msr [76]. The angular acceptance of each of these detectors is about $\pm 10^\circ$. Together, the Si detectors form the self-supporting BSiB sphere of 20 cm in diameter. For the present experiment, six positions in the BSiB detector array, selected at polar angles of 30° , $2 \times 75^\circ$, $2 \times 105^\circ$, and 150° , have been equipped with 4-element Si/CsI(Tl) detector telescopes. Each telescope consists of a stack of three ΔE Si detectors with thicknesses of 25–27 μm , 80–90 μm , and approximately 1000 μm , backed by a 7-cm thick CsI(Tl) crystal of 4 cm in diameter. A circular collimator in front of the 80- μm thick Si detector with a diameter of 19.5 mm defines the geometrical acceptance of the detector telescopes to values of about 21 msr.

2.2. Beam definition and monitoring

As illustrated in Fig. 1, about 11 m upstream from the target, the proton beam passes through a 0.3-mm thick and 20 mm in diameter plastic scintillator (S_1) read out by a fast photomultiplier. This fast scintillator detector provides a start signal for the time-of-flight (TOF) measurements (see Section 2.4) and is also used to count the number of incident beam protons. Additional scintillator detectors (\bar{S}_3 – \bar{S}_8), installed about 100 cm upstream from the target, are employed to identify and reject off-axis beam protons. The collimators define an accepted proton beam converging to a focus of about 2–3 mm diameter at the target position in the centre of BSiB. Ancillary downstream scintillators (S_{10} – S_{14}) are utilised to align and monitor the beam direction and the focal point.

During the data taking period, the event acquisition was enabled and triggered whenever a beam proton was detected by S_1 in coincidence with other detector signals. Consequently, protons that did not pass through S_1 do not disturb the cross section measurements, even if they induce a reaction in the target. Off-axis protons that traverse the S_1 detector at an angle to the

beam axis large enough to miss the target, are identified by the active collimator system. The yield of such beam protons was determined from “inclusive” data, which were taken periodically during the experiment. For example, every 10^5 th proton counted by the S_1 detector was used to start the acquisition without any further condition.

The accuracy in counting the number of incident protons directly contributes to the total error of the experimental cross sections. The scintillation detector S_1 which provides the primary proton count in the present experiment, was inhibited during the busy time of the data acquisition. This dead time with typical values of about 5–8% was continuously monitored during the runs. The proton beam admissible for a precise determination of absolute production cross sections was limited to moderate intensities of $< 1.5 \times 10^5$ pps. On the other hand, achieving meaningful statistics for LCPs and IMFs measured by the 6 detector telescopes, required data taking runs also at much higher intensities, i.e., at about $4\text{--}7 \times 10^6$ pps. For these measurements, the data acquisition was started independently of S_1 by at least one charged particle detected by BSiB or by telescopes. Thus, random coincidences between the signals of the BNB and the S_1 detector did not contribute to the acquisition dead time, and the effective number of events accumulated during the high-intensity runs was similar to that at the measurements with lower beam intensities. The data from the high-intensity runs were normalised with the help of the He yields measured with the BSiB, as will be described below in Section 2.4.2.

2.3. Targets

The targets of natural isotopic composition used in the present experiments were self-supporting metallic films of $1\text{--}10\text{ mg/cm}^2$ thickness, prepared by mechanical rolling. They were glued onto 0.2-mm thin, $25 \times 27\text{ mm}^2$ rectangular aluminium frames with a circular aperture of 20 mm diameter. The targets were positioned in the centre of BSiB by means of a movable target ladder. The ladder carried up to four target frames glued to a 14-cm long Al “flag-pole” with a $0.5 \times 5\text{ mm}^2$ cross section. Most of the telescope data were taken in runs with high beam intensities and with the target plane orientated at an angle of $\vartheta_T = 45^\circ \pm 5^\circ$ with respect to the beam axis. The absolute measurements, however, were performed with low beam intensities and with the target plane perpendicular to the beam ($\vartheta_T = 90^\circ$) thus minimising systematic uncertainty of the effective target thickness.

A precise determination of absolute cross sections depends crucially on how well the actual target thickness is known. In the present work, three independent methods have been applied to determine target thicknesses and associated uncertainties. Initially, the thicknesses of the $23 \times 24\text{ mm}^2$ target films were determined by just weighing. In this method, only the film thicknesses averaged over the whole target surface are determined. More precise, differential information on target thickness and uniformity was obtained with a second method relying on energy-loss measurements with alpha particles. In these measurements, a collimated ThC source was employed, emitting 6.06 MeV and 8.76 MeV alpha particles in the decays of ^{212}Bi and ^{212}Po , respectively. The source collimator with a diameter of 4 mm defined a surface area approximating the proton beam spot on the target. The target uniformity was investigated by scanning the target surface. The thicknesses were then deduced from the measured energy losses and alpha particle stopping powers which have been calculated with the computer code TRIM [77]. Generally, for alpha particles with energies of 3–9 MeV, the systematic uncertainty of the used stopping power data is evaluated to be 3–5% [78,79]. In most cases, discrepancies between target thicknesses determined by this latter method and simple weighing were found to be smaller than 4%. The results are listed in Table 1.

Table 1

Targets used in the present measurements. The layer thicknesses have been determined by weighing (Δx_w) and by energy-loss measurements (Δx_α) with alpha particles. The deviations between the results of both methods are given. The non-uniformity has been investigated by energy-loss measurements afar from the target centre. The overall error of the layer thickness determination is given in the last column, summarising the experimental and systematic contributions as well as the uncertainty due to target non-uniformity

Target	Target thickness			Non-uniformity (%)	Overall error (%)
	Δx_w (mg/cm ²)	Δx_α (mg/cm ²)	$\frac{\Delta x_\alpha - \Delta x_w}{\Delta x_w}$ (%)		
Al	1.39	1.33	−4	—	8.7
Ti	2.47	2.42	−2	1	5.3
Fe	1.75	1.74	−1	3.5	6.3
Ni	1.76	1.73	−2	1	5.3
Cu	1.47	1.46	−1	2	5.6
Zr	2.12	2.10	−1	3	6.0
Ag	4.02	4.19	4	3.5	6.2
Ho	5.01	5.22	4	6	7.9
Ta	7.64	7.48	−2	1.5	5.3
W	9.72	9.81	1	2.5	6.3
Au	5.89	6.05	3	2.5	5.7
Pb	6.28	6.34	1	—	8.7
Th	5.90	6.17	5	2.5	5.7

In a third method, the total neutron yields measured with BNB for the employed targets of 1–10 mg/cm² thickness were compared with similar measurements for much thicker (0.5–10 g/cm²) and more uniform (2–3%) targets. Such a comparison, however, can be performed with sufficient accuracy only for heavier targets. For targets at least as heavy as Ag, the measured mean neutron multiplicity is high enough, such that errors due to the background contribution are tolerable even for the mg-thin targets. For Ag, W, Au, and Pb, the results obtained with this third method confirm, within 1.5%, the values for target thicknesses determined with the above mentioned energy-loss method. The Ho target made an exception. The resulting discrepancy of $6.3 \pm 0.6\%$ between the two methods is ascribed to the large non-uniformity (6%) of the Ho target. Indeed, a small shift of the beam spot afar from the target centre by a few mm cannot be definitely excluded during the data taking runs. Consequently, the effective thickness may differ for non-uniform targets from that of the energy-loss measurements in the centre.

Following the argumentation above, a target thickness increased by 6% relative to the energy-loss measurement is applied for the determination of the cross sections in the reactions with the Ho target. For all other targets, however, the thicknesses derived from the energy-loss measurements were used, as given in the third column of Table 1. The overall uncertainties of the target thicknesses with values between 5.3% and 8.7% (including non-uniformity) contribute considerably to the total error of the present absolute cross section data.

2.4. Particle identification and energy thresholds

This paper reports on cross section measurements performed with both, the 4 π Silicon Ball BSiB and the set of six Si/CsI(Tl) detector telescopes. The following discussion relates to methods of particle identification, various associated sources of systematic uncertainties, thresholds, as well as to corrections to the measured data. Further details are given in Ref. [76].

Table 2

Experimental lower (E_{low}) and upper energy thresholds (E_{upper}) of the present cross section measurements with BSiB and telescopes

Particles	BSiB		Telescopes	
	E_{low} (MeV)	E_{upper} (MeV)	E_{low} (MeV)	E_{upper} (MeV)
^1H	2.0	26 ± 4	4.5*	150
^2H	2.0	51 ± 6	6.0*	200
^3H	2.0	77 ± 7	7.0*	250
^3He	2.0	100	7.0	300
^4He	2.0	100	7.0	300
^6He			7.0	62
Li			10.5	100
Be			16.0	100

* For the telescope measurements of the hydrogen isotopes, the given lower thresholds result from particle identification with the energies $\Delta E_{80}-E_{1000}$, whereas the low-energy cut-off for the other detected particles is determined by $\Delta E_{25}-E_{80}$.

Particle identification with BSiB detectors was obtained by means of energy and time-of-flight measurements; for the Si/CsI(Tl) telescopes, the $\Delta E-E$ method provided this information. One advantage of the E -TOF method consists in an energy threshold of only about 2 MeV, considerably lower than those of the telescopes (see Table 2). On the other hand, identification of charge and mass with the telescopes is much superior to the E -TOF method. It is also noteworthy that the energy range covered for the hydrogen particles is extended up to at least 100 MeV by the telescope measurements while the high geometrical acceptance of BSiB allows to achieve sufficient statistics even in absolute measurements with moderate beam intensities. Thus, to some extent, the measurements with both detectors complement one another.

2.4.1. Measurements with BSiB without isotopic resolution

Due to the short TOF pathlength of 10 cm (the inner radius of BSiB) BSiB does not provide isotopic resolution for LCPs. Hydrogen and helium particles, however, are separated from each other and are clearly discriminated from IMFs, fission fragments and heavy residues. Additional information on the particle species was obtained by utilising the pulse shape discrimination (PSD) of the detector signals [76].

Since the E -TOF method is sensitive to the mass but not to the particle charge, it appears impossible to separate ^3He from ^3H at energies below the tritium punch-through energy of about 12 MeV in a 500- μm thick Si detector. However, this particle identification threshold can be reduced to about 9 MeV by utilising the PSD signal (see Fig. 7 in Ref. [76]). Furthermore, in the energy region below, the plasma delay increases the apparent TOF of ^3He by about 1 ns compared to ^3H thus introducing a deviation between the two E -TOF particle branches. The ^3He fraction of incorrectly as hydrogen identified particles was estimated with the help of simulation calculations, which consider experimental resolutions and the TOF shifts due to plasma delay. The thus obtained corrections increase the measured helium ($^3\text{He} + ^4\text{He}$) cross section by 7.5%, 5.0%, and 2.4% for Al, Fe, and Ag targets, respectively. Correspondingly, the hydrogen ($p + ^2\text{H} + ^3\text{H}$) production cross sections were decreased by 3.2%, 1.5%, and 0.8% of the measured values. These corrections decrease with target mass due to the increasing Coulomb barrier, which tends to move an increasing fraction of the ^3He spectrum beyond the tritium punch-through energy.

The low Coulomb barrier of light nuclei, such as Al, results also in a considerable cut-off of the hydrogen and helium yields by the lower detection thresholds. This is demonstrated for helium in Fig. 2 where the measured angle-integrated energy spectra (dots) are compared with simulation calculations (shaded histograms) using the codes INCL2.0 and GEMINI. It is worth noting that a considerable fraction of the helium production as simulated by GEMINI proceeds through the primary evaporation of the unstable ^5He , thus contributing in particular to the low-energy part of the calculated spectra. In order to have a well defined lower threshold, an off-line cut-off at 2 MeV is employed for all detectors. The simulated data are filtered with the acceptance of the active BSiB detectors and include also the energy loss in the target.

The calculated and experimental spectra have been normalised in the energy region indicated by the two vertical dashed lines. As seen in Fig. 2, considerable yield is found below 2 MeV only for the lighter targets, resulting, e.g., in values of 17% and 3% for the measured helium cross section of Al and Fe, respectively. For hydrogen, the corresponding corrections are 9% and 4%. In addition to these corrections, the production cross sections as measured with BSiB were corrected for double hits, geometrical efficiencies, background as measured with empty target frames, and dead times (see Ref. [76]).

The lower energy threshold defines also upper energy cut-offs for punched-through particles, which depend on the effective depletion depth of each Si detector. Since these thicknesses var-

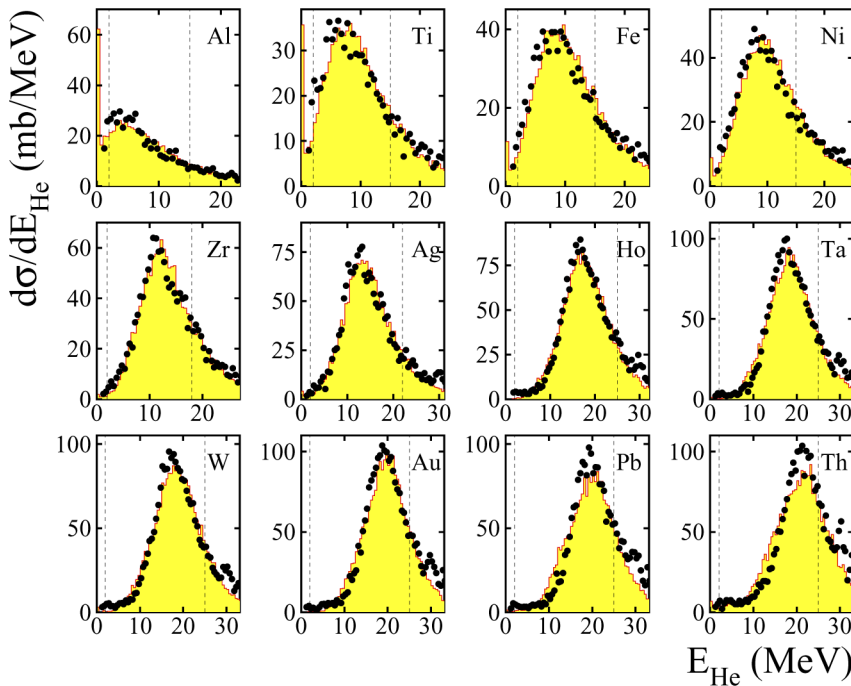


Fig. 2. Comparison of the angle-integrated helium energy spectra as measured with the BSiB detectors (dots) and as calculated with the codes INCL2.0 and GEMINI (shaded histograms). The dashed vertical lines define energy ranges of evaporated particles which were employed to normalise the simulated spectra to the measured yields. The helium yield below the lower threshold has been determined from the simulated spectra to correct for the corresponding counting losses of the measurements. Particle absorption within the target layer contributes to the yield in the first energy bin (see, e.g., histograms of Al and Ti).

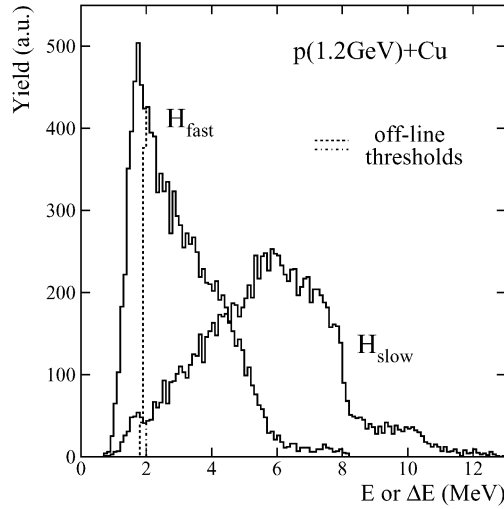


Fig. 3. Energy spectra of stopped (H_{slow}) and punched-through (H_{fast}) hydrogen ions accumulated with BSiB in the reaction $p(1.2 \text{ GeV}) + \text{Cu}$. The lower off-line thresholds are indicated by the dashed lines. For punched-through hydrogens (H_{fast}), the lower threshold corresponds to upper cut-off energies at about 26 MeV for protons, 51 MeV for deuterons, and 77 MeV for tritons.

ied between 440 and 500 μm , the data have been analysed with lower off-line energy thresholds adjusted for each detector separately in order to define the upper cut-off energies uniformly. This procedure was important for the hydrogen particles, in particular, for protons. In Fig. 3, the energy and energy-loss spectra are displayed for stopped (H_{slow}) and punched-through (H_{fast}) hydrogen ions. Since a large spectral range of punched-through protons is compressed into a small energy-loss bin, any uncertainty in the cut-off energy results in a considerable error in the derived integral yield. Corresponding to the upper cut-off energies, the measured yield for hydrogen ions σ_H , extrapolated to zero energy, represents the sum of the cross sections of protons, deuterons, and tritons $\sigma_H = \sigma_p(0\text{--}26 \text{ MeV}) + \sigma_d(0\text{--}51 \text{ MeV}) + \sigma_t(0\text{--}77 \text{ MeV})$. For helium ions, the spectrum is measured up to about 100 MeV, representing almost the full energy range (see also Table 2).

In Fig. 4, experimental angular distributions are shown for He ions, as measured with the BSiB detectors with the target at $\vartheta_T = 90^\circ$ (top panel) and $\vartheta_T = 45^\circ$ (lower panel). In the case of a perpendicular orientation to the beam axis, detectors near $\vartheta_T = 90^\circ \pm 10^\circ$ are “shadowed” due to considerable energy loss in the target. Their yield has therefore been omitted in the fit of the angular distributions with a $\cos(\vartheta)$ function

$$Y(\vartheta) = P_0(1 + P_1 \cos(\vartheta) + P_2 \cos^2(\vartheta)). \quad (1)$$

The data shown in the lower panel are measured with pulse-shape discrimination (PSD) which provides helium identification for high-intensity measurements in the energy range of 11–58 MeV (see Section 2.4.2). Thus, the contributions from more direct helium emission is slightly reduced, resulting in a somewhat decreased forward-backward asymmetry. However, it is clearly seen that the function defined by Eq. (1) is well suited to fit the experimental data. Angle-integrated cross sections were determined from the integral of the above expression over $4\pi \text{ sr}$, $Y_{4\pi} = 4\pi P_0(1 + P_2/3)$.

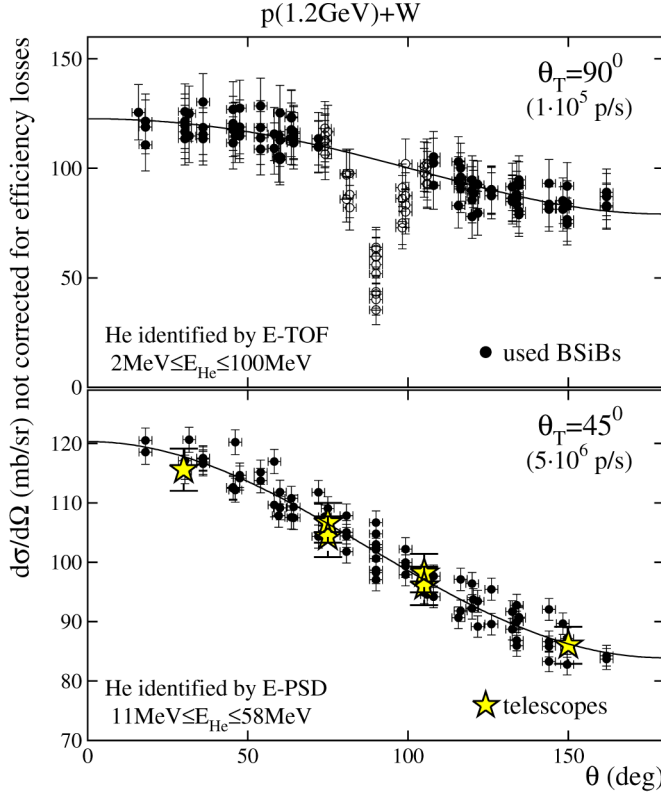


Fig. 4. Angular distribution of helium ions from the reaction $p(1.2 \text{ GeV}) + W$ as measured with BSiB detectors (circles) and telescopes (stars). The data points in the top panel were obtained with the target plane perpendicular to the beam axis and a low proton beam intensity of about 10^5 pps. The measurement plotted in the lower panel was performed with the target rotated to 45° and a beam of about 5×10^6 pps. The results of the BSiB detectors with positions close to the target plane are included in the top panel (open circles) but omitted in the bottom panel. The lines fit the BSiB data (filled circles) with the function of Eq. (1). Note the different vertical scales of both panels.

2.4.2. Telescope isotopic-yield measurements

As mentioned above, measurements employing the Si/CsI(Tl) detector telescopes suffered from energy thresholds that are considerably higher than those of the BSiB silicon detectors used with an E -TOF method. The actual lower energy thresholds and upper cut-off energies are given in Table 2 for the measured hydrogen and helium isotopes as well as for Li and Be. These thresholds correspond to energy losses in the Si detectors the charged particles have to pass through. Hydrogen events are effectively detected only in presence of signals from the 1000- μm thick Si detector. Consequently, the thresholds for hydrogen particles advert to energy losses in a total layer of $25 + 80 \mu\text{m}$ silicon while the low-energy thresholds of the other particles are related to the 25- μm thick Si detector element alone. In order to correct the measured yields for the corresponding low-energy thresholds, the experimental spectra were extrapolated to zero energies applying a procedure as already described in Section 2.4.1. Again, the yields below the thresholds are largest for light target nuclei with low Coulomb barriers, such as Al. Here, the corrections amount to 13–33%, for $^1,2,3\text{H}$, and 20–50%, for $^3,4,6\text{He}$. In the case of Fe, the corresponding values are 12–20% and 7–23%, respectively. For Ho and heavier targets with high

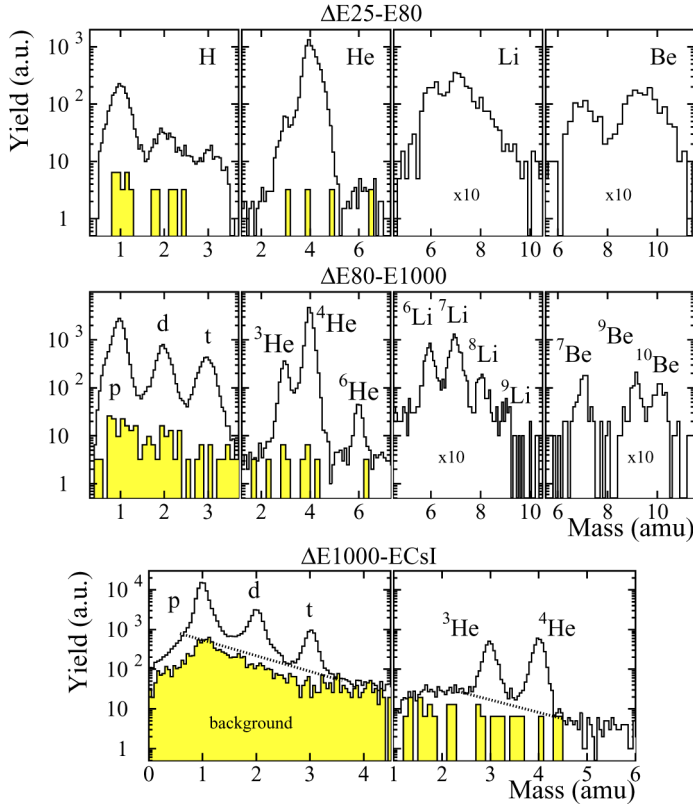


Fig. 5. Mass spectra of H, He, Li, and Be ions as measured with the ΔE – E combinations of the telescope detectors 25–80 μm (ΔE_{25-E80}), 80–1000 μm ($\Delta E_{80-E1000}$) and 1000 μm –7 cm ($\Delta E_{1000-ECsI}$). Events of all data taking runs have been accumulated. The background contributions due to reactions outside the target are shown by gray histograms.

Coulomb barriers, the corrections are less significant and amount to only 1–2%. For Li and Be, the yield losses below the lower thresholds are discussed more in detail in Section 3.2.4.

The mass spectra of hydrogen, helium, lithium, and beryllium isotopes are shown in Fig. 5 as obtained with the following three different combinations of ΔE and E detectors: for the lowest particle energies, the 25- μm and 80- μm thick silicon detectors were used (ΔE_{25-E80}), the higher energies are measured by the silicon detectors of 80 μm and 1000 μm thickness ($\Delta E_{80-E1000}$) as well as by the combination of the 1000- μm thick silicon detector and the 7-cm thick CsI(Tl) scintillator ($\Delta E_{1000-ECsI}$). The mass resolution of the last two combinations is sufficient to separate all isotopes while in the case of ΔE_{25-E80} the separation is marginal, in particular, for Li and Be. The systematic error for the identification of ${}^6,{}^7\text{Li}$, ${}^8\text{Li}$, ${}^9\text{Li}$, and ${}^9,{}^{10}\text{Be}$ in the mass spectrum of ΔE_{25-E80} was estimated to be 10%, 20%, 30%, and 15% of the measured yields, respectively.

Effort was spent to account for the contamination of ${}^3\text{He}$ by the intensive yield of ${}^4\text{He}$. This contribution has been determined from the data summed over all target runs. The summation was required to fit the data with sufficient statistics by two Gaussians and an additional component for the low-mass tail of ${}^4\text{He}$. Depending on the experimental resolutions of the detector telescopes, corrections of 30–60% and 12–20% have been determined for the ${}^3\text{He}$ yields in the mass spectra

of $\Delta E_{25}-E_{80}$ and $\Delta E_{80}-E_{1000}$, respectively. The separate measurements have been corrected with reference to the total number of detected ^4He in order to consider the actual $^3\text{He}/^4\text{He}$ ratio for the reactions with different targets. The uncertainty of this correction has been estimated to be about 50% of the reduction and constitutes the largest error contribution of the ^3He cross sections.

The background in the mass spectrum as measured in runs with an empty target frame is indicated by the shaded histograms in Fig. 5. Background corrections applied to the telescope data of the detector elements $\Delta E_{25}-E_{80}$ or $\Delta E_{80}-E_{1000}$ amount typically to <1% for H and <0.5% for He. Larger corrections, 2–3% for protons, and 5–6% for deuterons and tritons, were applied to the measurements with the thinnest targets, i.e., to the Al, Fe and Cu data. The background for the detection of Li and Be isotopes was negligible.

The measurement of energetic particles involves the CsI(Tl) elements of the detector telescopes. Because of the sensitivity to and the high light-output for neutrons and γ -rays in CsI, the high-energy parts of particle energy spectra suffer from higher background levels. As seen in Fig. 5, the empty target frame measurement does not completely account for the background under the prominent peaks. This discrepancy indicates the presence of background produced by reactions in the target. Consequently, the effective total background had to be estimated by empirical assumptions about the behaviour of the background distributions within the mass spectra. With a function as indicated by the dashed lines, adopted background levels were 5–33% for protons, 7–40% for deuterons, 8–53% for tritons, 10% for ^3He , and 5% for ^4He . In the case of the hydrogen isotopes, the largest corrections again correspond to the measurements with Al, Fe, and Cu targets, and the smallest to the heavy targets, i.e., from Ag to Th. An uncertainty of 30% of the above corrections has been taken into account in the cumulative error calculation of the cross section values.

As mentioned in Sections 2.2, the telescope data were measured at proton beam intensities as high as $(4-7) \times 10^6$ pps. Since for these high-intensity beams counting of the incident protons is affected by considerable dead-time losses, the telescope yields had to be renormalised in order to deduce absolute cross sections. This normalisation procedure was performed employing the yields of He measured for kinetic energies between 11 and 58 MeV. In this energy range He particles were identified with BSiB detectors using pulse-shape discrimination (PSD) with negligible dead-time instead of the time-of-flight method [76]. Renormalisation factors were derived from the angle-integrated BSiB data taken at low and at high beam intensities for each target. This procedure effects both, different beam intensities as well as effective target thicknesses resulting from different orientations (45° and 90°) of the target plane with respect to the beam axis. The error associated with the above beam normalisation procedure was estimated to about 2%.

The He yields identified by E -PSD method have also been applied to verify the solid angles of the telescopes experimentally. For the first two telescope detector elements ($25-80\ \mu\text{m}$), the actual solid angles have been precisely determined from a comparison with regular BSiB detectors at neighbouring polar angles, using the respective He yields measured with heavy targets and the precisely known solid angles of the BSiB detectors [76]. The obtained solid angles were found to deviate from the nominal values only by a few percent. However, smaller solid angles were determined for the second and third detector elements $\Delta E_{80}-E_{1000}$ and $\Delta E_{1000}-E_{\text{CsI}}$. Additional efficiency losses are due to “double hits”, which in case of the CsI detectors were also generated by neutrons and γ -rays. The reduced geometrical efficiencies for the detector elements $\Delta E_{80}-E_{1000}$ and $\Delta E_{1000}-E_{\text{CsI}}$ have been taken into account in the data analysis applying typical corrections of about 10% and 25%, respectively, to the measured yields. An error of 30% was estimated for this correction.

A linear and particle-independent energy calibration has been obtained for the Si detectors by measurements with ^4He sources [76] combined with an analysis of the punch-through energies for the different particles. Energy calibrations of the CsI detectors have been performed separately for p, d, t, ^3He , and ^4He with reference to the energy losses in the 1000- μm thick Si detectors in front of the respective CsI crystals. The CsI detector calibration data have been fitted with polynomial functions. However, it turns out that, for the most part, the light output response of the CsI detectors is rather linear with particle energy. Differences in the CsI detector response for different particle species are pronounced only at relatively low energies. For high-energy hydrogen particles with very low energy losses in the 1000- μm thick Si detectors, the CsI punch-through energies were also used for the energy calibration. For the present 7-cm thick CsI crystals, these energies were calculated as 160 MeV for protons, 210 MeV for deuterons, and 250 MeV for tritons.

The statistical errors of the production cross sections derived from the telescope data amount typically to 0.5–1.5% for p, d, and ^4He , to 1–3% for t and ^3He , to 5–8% for $^6,^7\text{Li}$, to 10–25% for ^6He , ^8Li , and $^{7,9,10}\text{Be}$, and to 20–50% for ^9Li . The total errors are calculated by quadratic summation of the various uncertainties.

3. Results

3.1. Data from 4π measurements with BSiB

Experimental results obtained in this work for hydrogen and helium production cross sections at $E_p = 1.2$ GeV are presented in Table 3, together with previously published data [9,25,27]. The present data were taken with the BSiB silicon detectors covering essentially the entire solid angle.

The measured cross sections have been extrapolated to zero particle energy, as described in Section 2.4.1. While the hydrogen cross sections listed in Table 3 are considerably restricted by upper cut-off energies, the present helium cross sections cover the whole energy range up to about 100 MeV. Thus, the figures obtained for the helium cross sections can be compared directly with earlier results, which were based on volumetric gas measurements without any energy cut-off. In Fig. 6, the present helium production cross sections are confronted with such previous data [25,27].

While the present Pb data point lies, with overlapping error bars, about 17% above the earlier result of Ref. [27], significant discrepancies of 26–32% exist in the opposite direction between present and previous [25] results for Al, Fe, and Ni targets. These latter disagreements exceed the given error limits. They are possibly related to the fact that the earlier Al, Fe, and Ni data were obtained in measurements [25,27] utilising stacks of targets, in which secondary particles can induce additional reactions. This complication was avoided in more recent measurements of a Pb target [27], where a new “Mini-Stack” target configuration was employed.

In order to compare the present data with the production cross sections measured previously with NESSI [9], the latter data were also extrapolated to zero particle energies. Furthermore, the data originally reported in Ref. [9] have been reanalysed assuming a more correct, lower (–7.7%) geometrical efficiency [76] and applying a 1–3% double-hit correction that had previously been neglected. The corrected data of Ref. [9] are included in Table 3 (columns 3 and 5) and Fig. 6. Considering the errors of typically 7–9% as estimated for both measurements, the reanalysed helium cross sections are in reasonable agreement with the present results, but all former data are systematically lower by 6–14%. The earlier hydrogen cross sections, however, are 14–28%

Table 3

Production cross sections of hydrogen and helium as measured with BSiB at incident proton energy of 1.2 GeV. The cross sections are corrected for the counting losses below the lower energy threshold of 2 MeV, the upper cut-off energies are given in the table. The results of Enke et al. [9] have been corrected for a reduced geometrical efficiency of -7.7% [76], for counting losses due to double hits, and for lower energy cut-offs. The Pb value of Ref. [27] for the He production cross section σ_{He} in column 6 is obtained by $\sigma_{\text{He}} = \sigma_{\text{He}}^4 + \sigma_{\text{c}}/4$ with σ_{c} being the cumulative ^3He cross section quoted in Ref. [27]

Target	H production cross section		He production cross section		
	$0 \leq E_p \leq 26 \pm 4 \text{ MeV}$		$0 \leq E_{\text{He}} \leq 100 \text{ MeV}$		
	$0 \leq E_d \leq 51 \pm 6 \text{ MeV}$				
	$0 \leq E_t \leq 77 \pm 7 \text{ MeV}$				
	σ_{H} (b)	σ_{H} (b) [9]	σ_{He} (b)	σ_{He} (b) [9]	σ_{He} (b)
Al	0.70±0.07		0.38±0.05		0.479±0.022 [25]
Ti	1.39±0.09		0.55±0.04		
Fe	1.75±0.13	1.50±0.15	0.60±0.05	0.515±0.04	0.792±0.058 [25]
Ni	2.29±0.15		0.68±0.05		0.865±0.062 [25]
Cu	2.03±0.13		0.70±0.05		
Zr	2.60±0.17		0.86±0.06		
Ag	3.11±0.21		1.05±0.07		
Ho	3.13±0.26		1.25±0.10		
Ta	3.44±0.20	2.46±0.20	1.39±0.08	1.20±0.09	
W	3.39±0.23	2.47±0.20	1.39±0.09	1.25±0.09	
Au	3.55±0.22	2.68±0.20	1.50±0.09	1.39±0.10	
Pb	3.23±0.30	2.55±0.20	1.41±0.13	1.33±0.10	1.20±0.15 [27]
Th	3.35±0.21		1.55±0.10		
U		2.40±0.20		1.27±0.10	

smaller than the present data. This difference is considerably larger than expected by the quoted error limits; it is most likely associated with the lower effective thresholds for H_{fast} realised in the present experiment, as indicated in Fig. 3. In Ref. [9] the data were analysed without setting the low-energy thresholds separately for each detector as was done in the present work. Due to the reasons mentioned above we consider the new data obtained in the present experiment for LCP production in 1.2 GeV proton-induced reactions as the final results of the NESSI Collaboration, thus replacing the corresponding data from earlier experiments published by Enke et al. [9].

In Fig. 6, the total production cross sections of He ($^3\text{He} + ^4\text{He}$) with energies between 0 and 100 MeV are also compared with results of various model calculations. Theoretical results obtained with the intra-nuclear cascade code INCL2.0 coupled to the evaporation code GEMINI are presented by the solid curve. As seen in this figure, the experimental data are systematically underestimated by the calculations. This finding can be ascribed to additional pre-equilibrium emission, a process which is not taken into account in INCL2 + GEMINI simulations. The pre-equilibrium contribution to the total production cross section amounts to about 5–20%, as will be discussed in Section 3.2.2. The data are also compared to predictions by the code LAHET [39] using the two evaporation models RAL and ORNL. Although LAHET describes reasonably well the neutron production in thick targets [10,73], the implemented models largely fail to describe the helium production, corroborating previous findings [9,80]. The calculations with the combination of the codes INCL4.2 [67] and KHSv3p [68,69] systematically underestimate the helium production for all investigated targets.

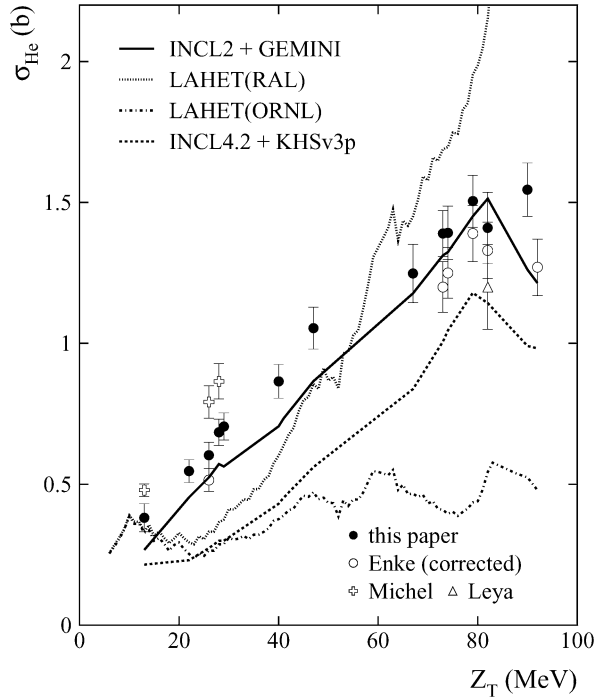


Fig. 6. Experimental (symbols) and calculated (lines) total He ($^3\text{He} + ^4\text{He}$) production cross sections as a function of the target atomic number Z_T . In addition to the present BSiB data (filled circles) previous data have been included from Enke et al. [9], Michel et al. [25], and Leya et al. [27]. The cross section data obtained with particle detectors have been corrected for lower detection thresholds. While the calculations with LAHET have been performed for all elements, the lines for INCL2 + GEMINI and INCL4 + KHSv3p connect the results for the same target nuclei as measured.

3.2. Data from measurements with the detector telescopes

3.2.1. Isotope-resolved cross sections of hydrogen and helium

As mentioned in Section 1, it is of particular interest for application purposes to know precisely the absolute integral H and He production cross sections. However, more detailed investigations require the knowledge of isotope-resolved data. The isotopic ratios, for example, give insight to evolving properties of excited nuclear matter and may be interpreted for signatures of particular reaction mechanisms. Production cross sections of separate isotopes are furthermore important for practical applications, e.g., to estimate the radiation exposure due to tritium decay. Finally, the upper cut-off energies for the hydrogen spectra as measured with BSiB complicate the use of this data for comparisons and estimates.

Isotope-resolved production cross sections from spallation reactions induced by 1.2 GeV protons are given in Tables 4 and 5 for hydrogen and helium, respectively. The measured yields have been integrated over particle energies from 0 to 100 MeV and over angles corresponding to the function of Eq. (1). Except for protons, the listed data σ_{tot} approximate well the total production cross sections, as illustrated by experimental energy spectra discussed further below. The summed cross sections of all three hydrogen isotopes differ considerably from the values given in Table 3 due to differences in the ranges of energy integration. For helium, however, the cross

Table 4

Measured production cross sections σ_{tot} of hydrogen isotopes with kinetic energies of $0 \leq E_{\text{H}} \leq 100$ MeV for 1.2 GeV proton-induced spallation reactions on targets between Al and Th. Separated pre-equilibrium cross sections σ_{PE} are also listed while the evaporative cross section σ_{EV} can be obtained from $\sigma_{\text{EV}} = \sigma_{\text{tot}} - \sigma_{\text{PE}}$

Target	^1H		^2H		^3H	
	σ_{tot} (mb)	σ_{PE} (mb)	σ_{tot} (mb)	σ_{PE} (mb)	σ_{tot} (mb)	σ_{PE} (mb)
Al	780 ± 120	390 ± 65	188 ± 33	73 ± 14	62 ± 14	12 ± 3
Ti	1750 ± 200	870 ± 100	393 ± 49	174 ± 22	122 ± 19	35 ± 6
Fe	1980 ± 250	830 ± 130	397 ± 55	167 ± 28	108 ± 17	36 ± 7
Ni	2750 ± 300	1170 ± 140	452 ± 54	217 ± 29	116 ± 15	46 ± 7
Cu	2300 ± 290	1000 ± 160	466 ± 63	220 ± 37	140 ± 22	47 ± 9
Zr	3200 ± 340	1570 ± 200	682 ± 73	347 ± 46	224 ± 26	90 ± 14
Ag	3770 ± 380	1790 ± 220	789 ± 81	380 ± 48	269 ± 29	114 ± 16
Ho	3990 ± 460	2420 ± 310	1030 ± 120	551 ± 71	458 ± 49	196 ± 28
Ta	4380 ± 430	2660 ± 310	1120 ± 110	621 ± 71	516 ± 46	225 ± 30
W	4260 ± 440	2600 ± 310	1090 ± 110	607 ± 74	498 ± 48	214 ± 30
Au	4670 ± 470	2940 ± 340	1230 ± 120	696 ± 82	551 ± 50	209 ± 27
Pb	4200 ± 510	2820 ± 380	1130 ± 130	655 ± 89	560 ± 64	253 ± 37
Th	4260 ± 470	3110 ± 360	1310 ± 130	770 ± 93	729 ± 68	296 ± 44

Table 5

Measured production cross sections σ_{tot} of helium isotopes with kinetic energies of $0 \leq E_{\text{He}} \leq 100$ MeV for 1.2 GeV proton-induced spallation reactions. Separated pre-equilibrium cross sections σ_{PE} for ^3He and ^4He are also listed while the corresponding evaporative cross sections σ_{EV} can be obtained from $\sigma_{\text{EV}} = \sigma_{\text{tot}} - \sigma_{\text{PE}}$

Target	^3He		^4He		^6He
	σ_{tot} (mb)	σ_{PE} (mb)	σ_{tot} (mb)	σ_{PE} (mb)	σ_{tot} (mb)
Al	45 ± 7	15 ± 2	316 ± 86	15 ± 3	1.6 ± 0.4
Ti	56 ± 6	26 ± 3	465 ± 82	41 ± 7	2.5 ± 0.4
Fe	66 ± 8	32 ± 4	511 ± 73	47 ± 9	2.4 ± 0.4
Ni	76 ± 8	37 ± 4	576 ± 74	60 ± 11	2.1 ± 0.4
Cu	72 ± 8	31 ± 4	596 ± 69	64 ± 12	1.3 ± 0.3
Zr	75 ± 9	42 ± 5	776 ± 67	90 ± 16	5.0 ± 0.8
Ag	85 ± 11	46 ± 5	1001 ± 84	102 ± 23	5.0 ± 0.7
Ho	74 ± 12	40 ± 6	1200 ± 110	161 ± 42	11.5 ± 1.3
Ta	77 ± 12	39 ± 5	1380 ± 100	190 ± 36	12.6 ± 1.3
W	78 ± 12	39 ± 5	1330 ± 110	170 ± 37	14.5 ± 1.5
Au	80 ± 12	41 ± 5	1440 ± 110	239 ± 68	14.3 ± 1.3
Pb	78 ± 13	42 ± 6	1350 ± 140	248 ± 55	16.2 ± 2.1
Th	85 ± 12	49 ± 6	1470 ± 120	224 ± 46	22.9 ± 2.2

sections listed in Table 3 and Table 5 are related to identical integration ranges and agree well within the experimental uncertainties, thus indicating the accuracy of the corrections applied.

Although deviations have been pointed out in Section 3.1 between total helium production cross sections of this paper and those reported in Ref. [25] the branching ratios $\sigma_{^4\text{He}}/\sigma_{^3\text{He}}$ determined in both measurements are in good agreement. While the present results listed in Table 5 yield to values of 7.0 ± 2.2 for Al, 7.7 ± 1.4 for Fe, and 7.6 ± 1.3 for the Ni target, the corresponding ratios of Ref. [25] amount to values of 8.2 ± 0.7 , 8.1 ± 0.8 , and 8.5 ± 0.9 , respectively. For the reaction with the Pb target, the agreement of the present $\sigma_{^4\text{He}}/\sigma_{^3\text{He}}$ branching ratio

(17.3 ± 3.5) with the corresponding value (12.2 ± 2.4) obtained in Ref. [27] is not as good. However, in this latter reference the ^3He cross section was corrected for the tritium decay by assuming $\sigma_t/\sigma_{^3\text{He}} = 3$, while the present measurement gives $\sigma_t/\sigma_{^3\text{He}} = 7.2 \pm 1.4$ for a Pb target (see Table 5). Using this $t/^3\text{He}$ ratio, the ^3He cross section reported in Ref. [27] would have to be reduced from (91 ± 13) mb to about (57 ± 12) mb, bringing the ^3He cross section to a value below the present result (78 ± 13 mb), and the $\sigma_{^4\text{He}}/\sigma_{^3\text{He}}$ branching ratio with 19.5 ± 5 closer to the data of the present work.

In the case of reaction with Au, the cross sections obtained for t , ^3He , and ^4He can be compared with corresponding data measured at incident energies of 1.8 GeV ($\sigma_t = 600 \pm 140$ mb, $\sigma_{^3\text{He}} = 200 \pm 80$ mb, and $\sigma_{^4\text{He}} = 1780 \pm 200$ mb [9]) and 2.5 GeV ($\sigma_t = 900 \pm 130$ mb, $\sigma_{^3\text{He}} = 210 \pm 40$ mb, and $\sigma_{^4\text{He}} = 1960 \pm 300$ mb [12]). The somewhat different energy ranges covered by the compared data do not disturb the conclusions substantially. As expected, the discussed cross sections increase with increasing proton energy, more gradually for ^4He , and more rapidly for ^3He .

3.2.2. Pre-equilibrium emission versus evaporation of LCPs

For comparison with model calculations, it is of particular interest to separate the contributions from pre-equilibrium emission and evaporation to the total production cross section. In the following, a decomposition of the experimental total cross sections into both components is discussed based on the shapes of the measured kinetic energy spectra. As an example, experimental spectra (dots) are shown in Fig. 7 for various hydrogen ($^1,^2,^3\text{H}$) and helium isotopes ($^3,^4\text{He}$) emitted in reactions with a Ta target at angles of 30° , 75° , and 150° . These spectra clearly feature two components—a low-energy evaporation peak and a high-energy tail due to particle emission prior to attainment of thermal equilibrium. The latter high-energy tail is weaker at backward than at forward angles. The spectral shape of the low-energy evaporative component is generally well described by the combined code INCL2 + GEMINI, as indicated by the shaded histograms.

The high-energy proton component is reasonably well reproduced by the calculations with the INC code, in particular, at forward angles. At backward angles, however, the simulation slightly underestimates the high-energy tail of the proton spectrum in a similar manner as already observed by Letourneau et al. [12] for the reaction $p(2.5 \text{ GeV}) + \text{Au}$. This behaviour is typical for all reactions studied in the present paper, almost independent on the target mass. The slope at higher energies of deuterons and ^3He resembles the proton spectra, while for tritons and ^4He the decrease at higher energies is obviously more rapid.

The evaporative parts σ_{EV} of the total production cross sections were deduced by first normalising the corresponding theoretical (INCL2 + GEMINI) evaporation spectra to the measured energy distributions, and then integrating them over energy and angle. The decomposition of the energy spectra into EV and PE components is shown more in detail in Fig. 8 by plotting the double differential cross sections at 30° with a *linear* scale and with higher energy resolution. The measured spectra are obviously disturbed at energies around 14 MeV for protons, 18 MeV for deuterons, and 21 MeV for tritons, corresponding to the passage of these particles through the 1000- μm thick Si detector. If a particle penetrates this detector but does not generate a signal in the CsI detector behind, it is treated as stopped and, consequently, its kinetic energy is underestimated. This hinders the comparison of the spectral shapes close to the punch-through energies. The measurement of the *integrated* particle yields, however, is not affected.

The gray histograms with the solid boundary indicate the simulated yields adjusted to the total inelastic reaction cross section from Ref. [66] while the dashed histograms are normalised to the integral of the measured data in between the vertical dashed lines. The corresponding scaling

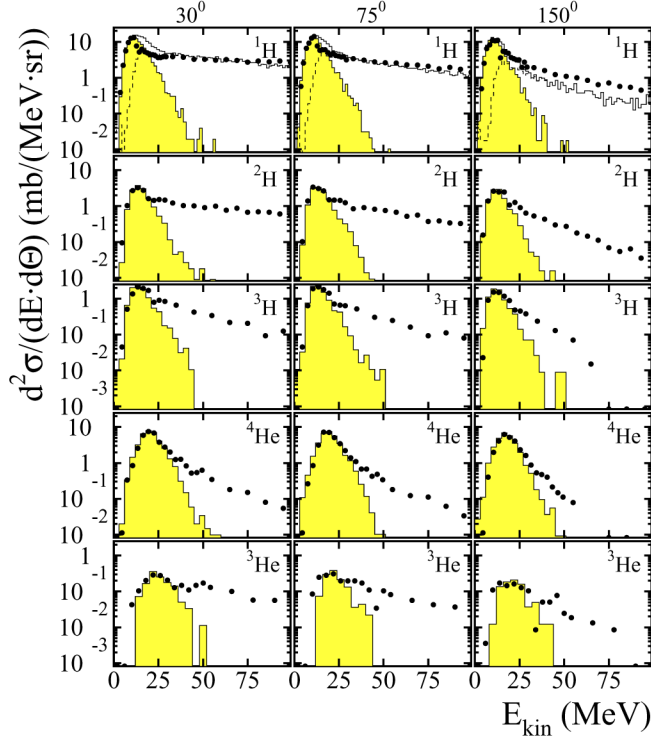


Fig. 7. Kinetic energy spectra of $^1,^2,^3\text{H}$, and $^3,^4\text{He}$ at 30° , 75° , and 150° for the reaction $p(1.2 \text{ GeV}) + \text{Ta}$. The shaded histograms display the calculated evaporation spectra normalised to the experimental data. In the upper panels (^1H) the calculated yield of promptly emitted protons (dashed histograms) is added to the evaporative contribution resulting in total spectra as shown by the solid histograms.

factors, only slightly different from 1, are given in the panels. The contribution from particle evaporation to the total yield above the normalisation range up to 100 MeV results in values of 10–20% for p, d, t, and ^3He , and about 40% for ^4He . An error contribution of 25% of the corresponding correction is estimated for this procedure.

It is apparent that the described approach is not completely free from arbitrariness. Indeed, the pre-equilibrium emission in the low-energy normalisation region is assumed to be negligibly small. On the other hand, the analysis of the zone with contributions both from evaporation and pre-equilibrium emission depends crucially on the reliability of the calculated evaporation spectra. However, due to the normalisation to the measured distributions, the deduced pre-equilibrium yields are influenced only by the *shape* of the calculated spectra but not by the calculated cross sections, in contrary to the analysis of Ref. [12]. Among the available computer codes the combination of INCL2 with GEMINI turned out to give the best fit to the experimental data in the evaporation region. The good agreement between the predictions of these codes and the measured data, demonstrated in the present paper for various observables, effectively supports the confidence to the calculated energy spectra.

A closer inspection of the proton spectra reveals that the calculated yield at energies between 10 and 20 MeV overestimates the experimental data. This discrepancy becomes more obvious in a *linear* plot where the calculated INC proton spectrum is compared to the difference

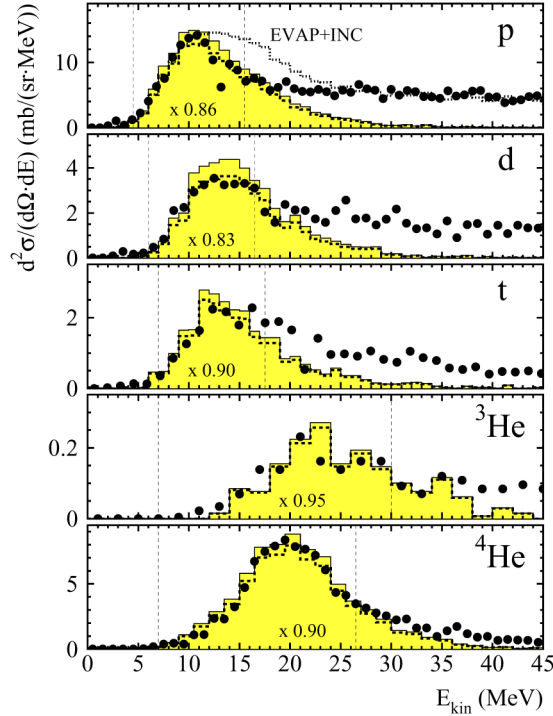


Fig. 8. Decomposition into contributions from evaporation and pre-equilibrium emission. Experimental kinetic energy spectra (symbols) as measured for the reaction $p(1.2 \text{ GeV}) + \text{Ta}$ at 30° are compared with spectra from INCL2 + GEMINI simulations (histograms). The range to fit the evaporative yields is indicated by vertical dashed lines. Simulated distributions above this region are used to estimate the evaporative portion which is subtracted from the measured yield to separate the contribution from pre-equilibrium emission. For further details see text.

spectrum of the measured proton energies and the evaporative component: $d^2\sigma_{\text{exp}}/(d\Omega dE) - d^2\sigma_{\text{EV}}/(d\Omega dE)$. The shape of the evaporative spectrum has been obtained from simulation calculations, the yield was normalised to the experimental data. Consequently, the resulting difference spectrum corresponds to protons which are not evaporated and thus emitted during the INC and/or PE phases. In the panels of Fig. 9 the difference spectrum is compared with the energy distribution calculated for INC protons, indicating an excess of the calculated yield at proton energies smaller than 20 MeV. In the evaporation region this excess causes a significant broadening of the simulated peak by up to about 5 MeV and a shift of the mean peak position to higher energies, clearly in contrast to the experimental observations (see also upper panel of Fig. 8). This finding is noticed both for heavy (Ta) and light (Ni) targets. The low-energy excess component seems to be largest at small emission angles. For measured low-energy neutrons emitted in the spallation reaction $1.2 \text{ GeV } p + \text{Pb}$, however, a good agreement with simulated energy spectra using the code INCL4 has been reported [59]. Neutron evaporation spectra from heavy targets are, however, less sensitive to contaminations from the INC part since their evaporative multiplicity is about ten times larger than for protons.

A surface coalescence model for cluster emission implemented into the codes INCL2 [12] or INCL4 [59] improves the agreement between calculated and measured proton spectra in the evaporation region. The applied coalescence formalism, however, also reduces the yield of INC

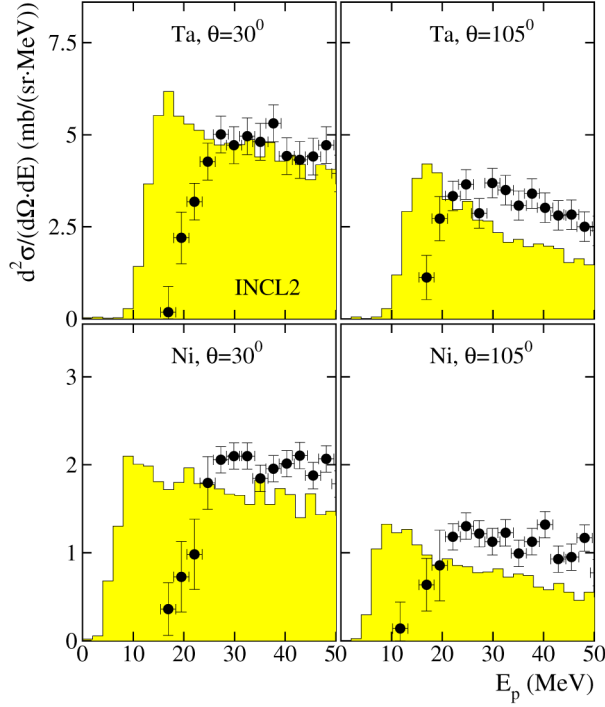


Fig. 9. Calculated INC proton spectrum (shaded histogram) and experimental difference spectrum $d^2\sigma_{\text{exp}}/(d\Omega dE) - d^2\sigma_{\text{EV}}/(d\Omega dE)$ for the targets Ta and Ni.

protons up to energies of about 150 MeV and thus adulterates the satisfactory agreement observed in absence of the coalescence model in the energy range above 40 MeV. The emission of very low-energy nucleons modelled by any INC approach is, a priori, questionable since the basic assumption of a small de Broglie wave length is violated for particles emitted with low velocities. In spite of this fact, i.e., restricted to the framework of the INC approach, the observed discrepancy between the simulated and measured proton spectra may be associated with assumptions for Coulomb barriers and emission probabilities used for proton emission in the INCL2 model.

The resulting PE cross sections $\sigma_{\text{PE}} = \sigma_{\text{tot}} - \sigma_{\text{EV}}$ are listed in Tables 4 and 5. Instead of plotting the production cross sections, the mean particle multiplicities $M_{\text{EV,PE}} = \sigma_{\text{EV,PE}}/\sigma_{\text{inel}}$ are shown in Fig. 10, where σ_{inel} is the total inelastic cross section [66]. Within a few percent the latter agrees numerically with the geometrical cross section, $\sigma_{\text{geo}} = \pi r_0^2 A_T^{2/3}$ with $r_0 = 1.26$ fm. The obtained multiplicities reflect the probability for emission of an EV or PE particle in an inelastic reaction. The mean evaporative multiplicities of tritons, deuterons, and ^4He are only weakly dependent on the target mass, they amount to about 0.15, 0.30, and 0.70, respectively. These multiplicities as well as the results for evaporated protons are satisfactorily described by the INCL2 + GEMINI calculations (see lines in Fig. 10), thus indicating that both the mean thermally equilibrated excitation energy after the prompt INC as well as its distribution to the different particle species (including neutrons) during the subsequent energy dissipation are correctly calculated. For the ^3He -multiplicity, the agreement is somewhat worse, but its strong decrease with target mass, quite different from the other isotopes, is correctly predicted by the calculations.

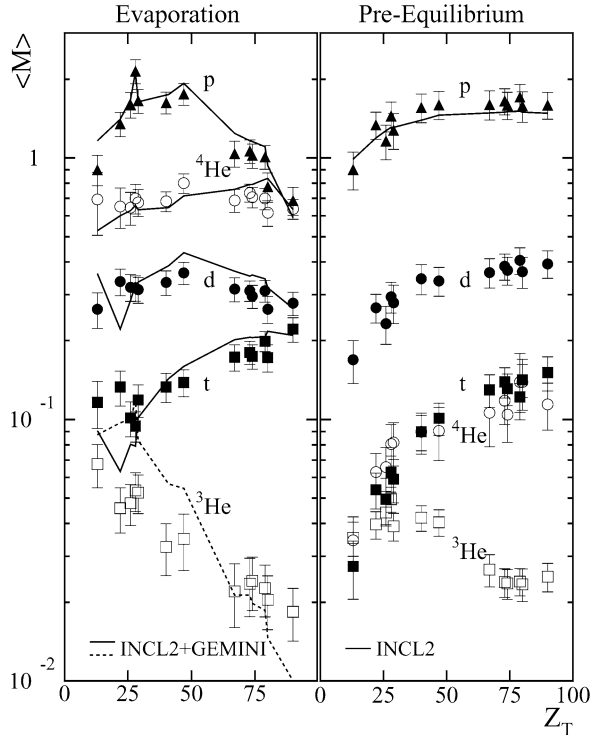


Fig. 10. Left panel: experimental (symbols) and calculated (solid and dashed lines) mean multiplicities of protons and composite particles as a function of the target atomic number Z_T . Right panel: experimentally deduced mean multiplicities of PE particles (symbols) with energies below 100 MeV. The solid line is the result of INCL2 calculations for protons with kinetic energies smaller than 100 MeV.

In the right panel of Fig. 10 the pre-equilibrium multiplicities are shown for particles with energies up to 100 MeV. It is interesting to note that the PE multiplicities of d, t, and ^3He are similar to that for the evaporation component. Whereas the multiplicity of evaporated ^4He is more than 4 times larger than that of evaporated tritons, the probabilities for PE emission of these two particle species are almost identical. The latter finding is difficult to understand within the framework of coalescence models [12,59], since the formation of ^4He requires the attachment of one more nucleon than needed for ^3H .

The relative contribution of PE emission amounts to 40–60% for deuterons and ^3He , 20–40% for tritons and only 5–20% for ^4He , where the lower and upper value applies to lighter and heavier targets, respectively (see Fig. 11). For the medium-mass and heavy targets, the relative contributions depend only weakly on the size of the target nucleus. They also depend only weakly on the bombarding energy as can be learned from the comparison with investigations at 2.5 GeV (data from Ref. [12] drawn in Fig. 11), 1.8 GeV [9], and much lower incident energy [32]. The LCP emission as a function of the deposited thermal excitation energy E^* has been studied in detail by Letourneau et al. [12]. Both evaporation and pre-equilibrium emission show the general behaviour that the particle multiplicities raise with increasing E^* . Since this increase is more rapid for the evaporated particles, the relative PE contribution is largest for reactions with a small amount of deposited E^* , in agreement with the result of Ref. [9].

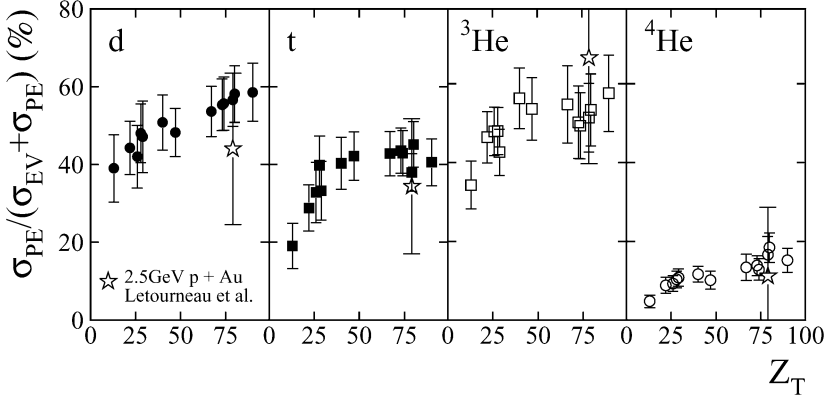


Fig. 11. Contributions of the pre-equilibrium emission relative to the total yield of light composite particles. The data measured for reactions with 1.2 GeV protons are plotted as a function of the atomic target number Z_T . For comparison, results from Ref. [12] are also shown.

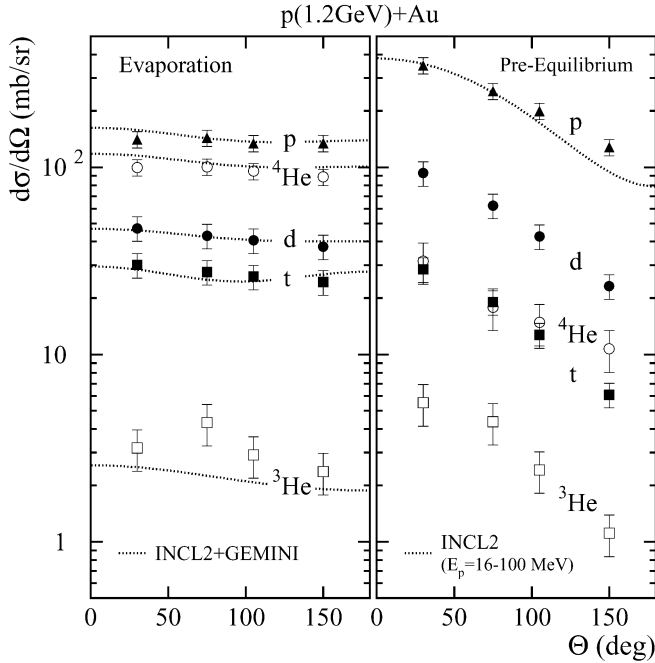


Fig. 12. Experimental (symbols) and calculated (dashed lines) angular distributions of evaporative (left panel) and pre-equilibrium (right panel) LCPs emitted in the reaction $p(1.2 \text{ GeV}) + \text{Au}$.

As mentioned above, the angular anisotropies in the laboratory system of evaporative and pre-equilibrium particles are quite different: the EV component is obviously more isotropic than the PE part. To demonstrate this fact more clearly, the angular distributions for both LCP components are shown in Fig. 12 as obtained in the reaction with the Au target: in the left panel, the EV components of various LCP species are compared with the results of INCL2 + GEMINI calculations (dashed lines). The observed small anisotropies are due to the recoil velocities of the emitting

residual nuclei after the prompt intra-nuclear cascade. The good agreement between experiment and calculation indicates that this recoil velocity is well predicted by the INCL2 code, as will be discussed in more detail in Section 3.2.3.

The angular distributions of the PE components, shown in the right panel of Fig. 12, exhibit as expected a much stronger anisotropy. They are very similar in shape, and the experimental proton data are well described by the INCL2 code, at least for proton energies between 16 and 100 MeV. The forward/backward intensity ratio varies between 3 and 6 for the LCPs, rather independent from the size of the target nucleus.

Within the framework of a coalescence model, the yields of PE composite particles are assumed to be correlated with the yields of fast cascade nucleons. Thus it is reasonable to analyse the ratio $\sigma_{\text{PE}}/\sigma_{\text{PE,p}}$, i.e., the measured cross sections σ_{PE} for the PE emission of composite particles in the energy range up to 100 MeV, related to the corresponding cross sections $\sigma_{\text{PE,p}}$ for the protons. This has been done in Fig. 13 for deuterons, tritons, and ^3He .

At intermediate energies, neutrons and protons are treated by the INC in a similar manner. Consequently, the ratio $n_{\text{INC}}/p_{\text{INC}}$ of n_{INC} neutrons and p_{INC} protons emitted during the INC cascade agrees with the ratio $N_{\text{T}}/Z_{\text{T}}$ of neutrons and protons composing the target nucleus. Following the description of a surface coalescence model [12,59], the formation of composite particles proceeds when a cascade nucleon is going to escape the nucleus and meets other nucleons at the nuclear surface close enough in phase space to condense. A deuteron, for example, is thus generated either by an INC neutron picking up a proton at the surface, or by a fast INC proton merging with a surface neutron. Thus, the ratio between the number of deuterons produced in such a manner to the number of cascade protons is expected to scale with the ratio $N_{\text{T}}/A_{\text{T}}$. This behaviour is exactly what we observe in Fig. 13 for the experimental data $\sigma_{\text{PE,d}}/\sigma_{\text{PE,p}}$. If, however, the

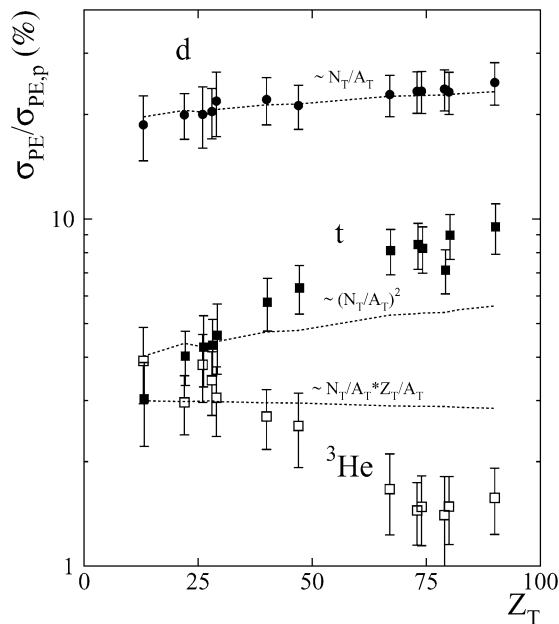


Fig. 13. Pre-equilibrium emission cross sections for deuterons (\bullet), tritons (\blacksquare), and ^3He (\square) divided by the cross section of energetic protons. The data (symbols) are obtained from the results of σ_{PE} as listed in Tables 4 and 5 for kinetic energies up to 100 MeV. The plotted lines are explained in the text.

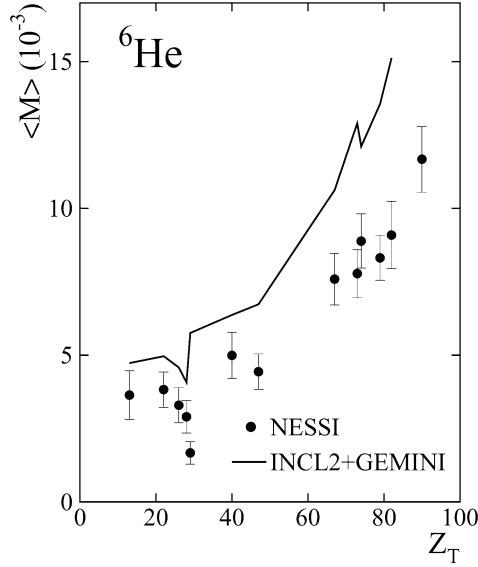


Fig. 14. Experimental (symbols) and calculated (solid line) mean ${}^6\text{He}$ multiplicities as a function of the target atomic number Z_T .

coalescence approach would be restricted to the interaction of cascade nucleons only (as, e.g., applied in Ref. [38]) then a much stronger dependency of $\sigma_{\text{PE,d}}/\sigma_{\text{PE,p}}$ would be predicted, since the total number of cascade nucleons increases with the size of the target nucleus. Similar estimates as discussed above for deuterons have been also adopted for the PE emission of tritons and ${}^3\text{He}$, relating the ratios of $\sigma_{\text{PE,t}}/\sigma_{\text{PE,p}}$ and $\sigma_{\text{PE,}{}^3\text{He}}/\sigma_{\text{PE,p}}$ to the composition N_T , Z_T , and A_T of the target nucleus (see dashed lines in Fig. 13, arbitrarily normalised to data points of light target nuclei). The agreement between the experimental data and the simple estimates is obviously not as good as for deuterons. The discrepancies could possibly be correlated with an enhanced n/p ratio at the surface of heavy target nuclei. However, for final conclusions comprehensive simulation calculations are required as have been announced in Ref. [59]. The ratio $\sigma_{\text{PE,}{}^4\text{He}}/\sigma_{\text{PE,p}}$ for ${}^4\text{He}$ (not shown in Fig. 13) results in values close to those of ${}^3\text{H}$. This finding is difficult to understand in the framework of a coalescence model consistent for all composite PE particles. Consequently, other descriptions are required for the observed ${}^4\text{He}$ yields.

Due to low statistics obtained for the halo nucleus ${}^6\text{He}$, it was not possible to separate PE and EV components. Hence, in Fig. 14 the total ${}^6\text{He}$ multiplicity is compared with the results of the INCL2 + GEMINI calculations. Obviously, the calculation overestimates the production of this neutron rich He isotope. It is interesting to note that the multiplicities strongly increase with increasing Z_T . This behaviour is similar to that of the neutron rich tritons as shown in Fig. 10 and, obviously, due to the larger neutron excess of heavier targets.

3.2.3. Excitation energy and linear momentum transfer

For the calculation of LCP cross sections discussed further above, it is essential that the energy dissipation in the initial intra-nuclear cascade is modelled correctly. Sensitive observables to investigate this subject are excitation energy and linear momentum transfer. For proton-induced spallation reactions up to 2.5 GeV it was shown in Refs. [9,12,13], that the experimentally deduced excitation energy distributions agree quite well with those predicted by INCL2 cal-

culations, whereas they differ from the results of calculations performed with the LAHET code [39], in particular, for higher proton energies and for heavy targets.

The discussion of the excitation energy *distributions* obtained from the present measurements will be subject of a forthcoming paper [81]. Here, for the time being, the analysis is restricted to the *mean* thermal excitation energy $\langle E^* \rangle$ deposited in the residual nucleus at the end of the intra-nuclear cascade. This observable was experimentally deduced, as described in Ref. [17], from the mean multiplicities of evaporated light charged particles (left panel of Fig. 10) and neutrons. The neutrons were measured separately with BNB [75] for targets ranging in thickness between 0.1 and 1.0 g/cm² [82]. The obtained mean excitation energies (solid squares) are plotted in Fig. 15 versus the atomic number Z_T of the target nucleus, together with the predictions (lines) of the simulation models INCL2.0 [64], INCL4.2 [67], and LAHET [39]. It is worth noting that the “efficiency” $\langle E^* \rangle / E_p$ of converting the kinetic energy (E_p) of the incident proton into excitation is only 6% for a nucleus as light as Al, increasing to 15% for a heavy nucleus such as Pb, while the balance is carried off almost completely by fast INC nucleons.

Obviously, the calculations with INCL2 agree relatively well with the experimental values between Al and Pb, although for heavier target nuclei the calculated mean excitation energies slightly overestimate the experimental results. Unlike the assumptions of the INCL2 model which simulates the nucleon–nucleon cascade within a compact sphere of homogeneous nucleon density, the advanced version of the Liège intra-nuclear cascade model INCL4 treats the nucleon

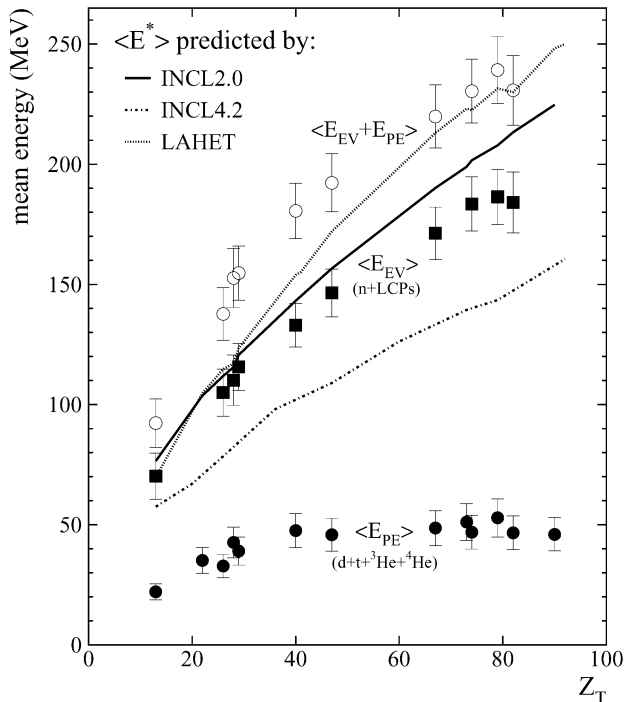


Fig. 15. Experimental mean energy $\langle E_{PE} \rangle$ carried off by PE emission of composite particles (solid circles) compared with the measured mean dissipated thermal excitation energy $\langle E_{EV} \rangle$ released by evaporated neutrons and LCPs (solid squares). The sum of both components is shown by open circles. The three plotted lines present predictions of the simulation codes INCL2.0, INCL4.2, and LAHET for the mean excitation energy $\langle E^* \rangle$ of the target remnant after the intra-nuclear cascade.

density in the target nucleus as described by a Saxon–Woods distribution, i.e., with a smooth transition at the surface of the nucleus. This development has been introduced to improve the reliability of the calculations for peripheral reactions. However, as to the mean thermal excitation energy, the results turn out to be in disagreement with the predictions of the older version INCL2 as well as with the present experimental data. The LAHET code with the BERTINI-type cascade model tends to overestimate the mean excitation energy, corroborating previous findings [9,80].

Some closer insight into the origin of this different behaviour is obtained from the analysis of the multiplicity distributions for neutrons and LCPs as plotted in Fig. 16. Two examples has been chosen as typical reactions with a light and a heavy target nucleus. The results of simulation calculations using the codes INCL2 + GEMINI, INCL4.2 + KHSv3p, and LAHET employing the RAL evaporation model are confronted with the experimental data as obtained from the measurements with BSiB and BNB. The calculated distributions have been filtered with the experimental conditions and are normalised to the total reaction cross section. The yields at medium and high multiplicities are obviously best reproduced by the simulations with INCL2 + GEMINI while discrepancies are noticed for simulated events with small neutron multiplicities, i.e., in the range of low excitation energies. The data measured at very low multiplicities are in good agreement with the predictions of the LAHET code. With exception of the neutron multiplicity in the reaction with Cu, the combination of INCL4.2 + KHSv3p underestimates the measured data in the range of large multiplicities. This finding is in agreement with the conclusion reported in [67] that this code underestimates the yield in the low-mass and low-charge side of the heavy residue distribution. The simulations with LAHET, in contrary, overestimate the yield of events with

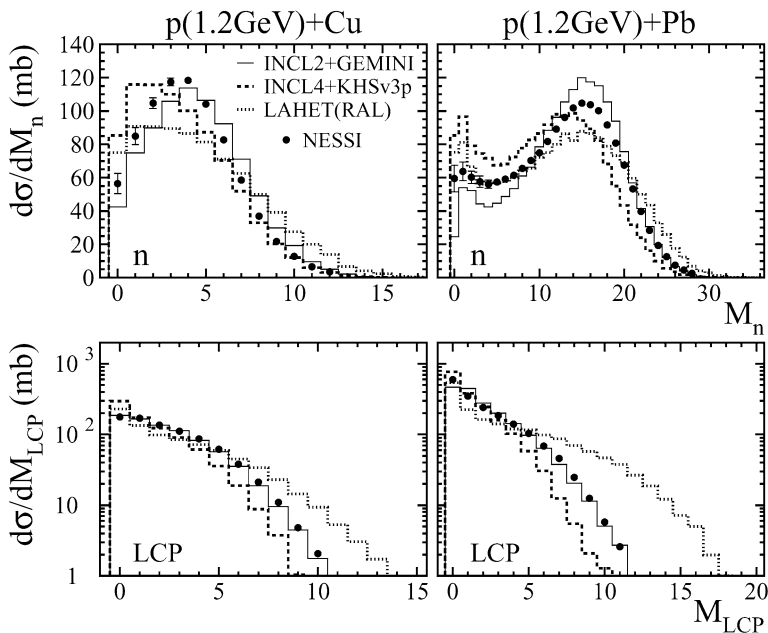


Fig. 16. Measured (symbols) and calculated (histograms) multiplicity distributions of neutrons (upper panels) and H + He (lower panels) obtained in 1.2 GeV proton-induced reactions with Cu (left) and Pb (right). The experimental data are corrected for background contributions, the calculated events are filtered with the experimental acceptance and detection efficiencies.

large multiplicities, in particular, as for the light charged particles, which are favourably emitted at higher excitation energies.

The calculated light-particle multiplicities are not completely defined by the thermal excitation energy of the decaying system as predicted by the INC codes. They are also influenced by the used evaporation model which governs the partition of the excitation energy to the different particle species and determines their kinetic energy. We recall that the code KHSv3p does not consider the emission of d, t, and ^3He and does not fit the low-energy region of measured He spectra [67]. The RAL evaporation model applied in LAHET scales the Coulomb barriers down with increasing excitation energies thus pushing the LCP emission and overestimating the low-energy region of the spectra. For the GEMINI code, however, a good agreement of the calculated kinetic energy spectra with measurements has been found in Refs. [9,11,12] as well as in the present work, thus making this code most suitable to extract the excitation energy distribution from the measured multiplicities.

While the intra-nuclear cascade model accounts for the energy carried off by energetic nucleons, it does not account for the energy released by PE emission of composite particles. Since in the present work both LCP multiplicities and energy spectra have been measured, one can determine the mean energy $\langle E_{\text{PE}}^i \rangle$ per PE composite particle of species i . Consequently, the total mean energy carried off by PE composite particles is then obtained by summing expressions of the form $\langle M_{\text{PE}}^i \rangle (E_{\text{PE}}^i + B_i)$ over $i = {}^2, {}^3\text{H}$ and ${}^3, {}^4\text{He}$, employing measured mean multiplicities $\langle M_{\text{PE}}^i \rangle$ of PE composite particles (see right panel of Fig. 10). Here, B_i is the binding energy to separate the composite particle i from the target nucleus. The largest contribution to this sum is due to deuterons, making up about 80% of the total. The result of this analysis is shown in Fig. 15 by solid circles. The open circles in this figure indicate the summed mean energies carried off by both components from light-particle evaporation and composite-particle PE-emission. About 20–25% of these summed mean energies is due to PE composite particles.

The deposited excitation energy is correlated with the magnitude of linear momentum transfer (LMT), which provides an independent cross check of the INC calculation. It is, however, noteworthy that the correlation between E^* and LMT in proton-induced spallation reactions is not as strongly pronounced as in medium-energy heavy-ion reactions [83]. The reason is that, in spallation reactions, the relatively broad angular distribution of the released fast INC nucleons result in a reduced longitudinal component of the total linear momentum, whereas the not interacting mass fraction of the projectile in heavy-ion incomplete-fusion reactions is almost completely carried off by particles emitted approximately with beam velocity and close to the beam axis.

In the following, the experimentally deduced mean LMT is compared with INCL2 predictions. The linear momentum transferred to the heavy residues can be deduced from the measured anisotropy of the angular distributions of evaporated particles. For example, the forward/backward asymmetry expressed by $Y(0^\circ)/Y(180^\circ) = (1 + P_1 + P_2)/(1 - P_1 + P_2)$ with P_1 and P_2 from Eq. (1) can be shown to be given by $((\langle v_i \rangle + \langle v_{\text{HR}} \rangle)/(\langle v_i \rangle - \langle v_{\text{HR}} \rangle))^2$. Here, the quantities $\langle v_{\text{HR}} \rangle$ and $\langle v_i \rangle$ are the mean centre-of-mass and particle emission velocities, respectively, with the latter obtained for evaporated particles of species i , e.g., from simulation calculations. It should be noted that this method tends to favour the higher centre-of-mass velocities, since, on average, the excitation energy and thus also the multiplicity of evaporated particles is larger for higher linear momentum transfers. Evaporated ${}^4\text{He}$ are the best suited particles for such an analysis. The small contribution of PE emission to the total ${}^4\text{He}$ yield allows to separate the evaporative fraction with low systematical errors. In Fig. 17, the centre-of-mass velocities $\langle v_{\text{HR}} \rangle$ of the heavy residues deduced from evaporated ${}^4\text{He}$ particles are presented by the solid circles and plotted versus target atomic number Z_T . The experimental results are seen

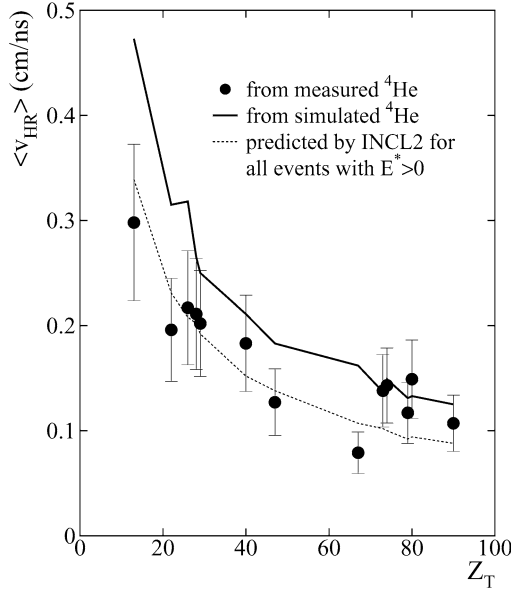


Fig. 17. Mean recoil velocities (filled circles) of heavy residues as extracted from the forward/backward emission asymmetry of evaporated ${}^4\text{He}$ versus the target atomic number Z_T . Calculated recoil velocities with and without weighting with the ${}^4\text{He}$ multiplicity are shown by the solid and dashed lines, respectively. For further explanations see text.

to lie between the INC calculations with (solid line) and without (dashed line) ${}^4\text{He}$ multiplicity weighting. In the first case, the simulated ${}^4\text{He}$ particles have been analysed in the same way as the experimental data, while the results “without ${}^4\text{He}$ multiplicity weighting” correspond to the HR velocities as calculated by INCL2 and as averaged over all simulated events with $E^* > 0$. Due to the pre-equilibrium emission of composite particles one would expect that the residue velocities are somewhat smaller than the INC predictions, where PE emission of composite particles is not taken into account.

3.2.4. Production cross sections for Li and Be

The detector telescopes used in the present NESSI experiment also allowed to measure the production cross sections for Li and Be isotopes. For these intermediate-mass fragments, the experimental low-energy cut-off occurs at considerably higher energies than for LCPs, i.e., at 10.5 MeV for Li, and 16 MeV for Be. Consequently, a larger fraction of the IMF spectrum is missing in the measured yield. To demonstrate the effect of this lower energy threshold, kinetic-energy spectra for Li and Be fragments are shown in Fig. 18 produced in reactions with a light (Ti), a medium-weight (Ag), and a heavy (W) target.

The shaded histograms in this figure are obtained from INCL2 + GEMINI simulation calculations normalised to inelastic reaction cross sections from Ref. [66]. The shapes of these spectra have been used to estimate the yields below the energy thresholds. To this aim, a normalisation of the simulated spectra to the measured data has been performed within the energy range of evaporated particles. For medium-weight targets, most of the evaporation peak is covered by the experimental data, and the simulated peak positions are in good agreement with the experiment. For the lighter targets, the normalisation is not as well defined, and only a small amount of the evaporative particles is detected above threshold. However, the good agreement of the differential

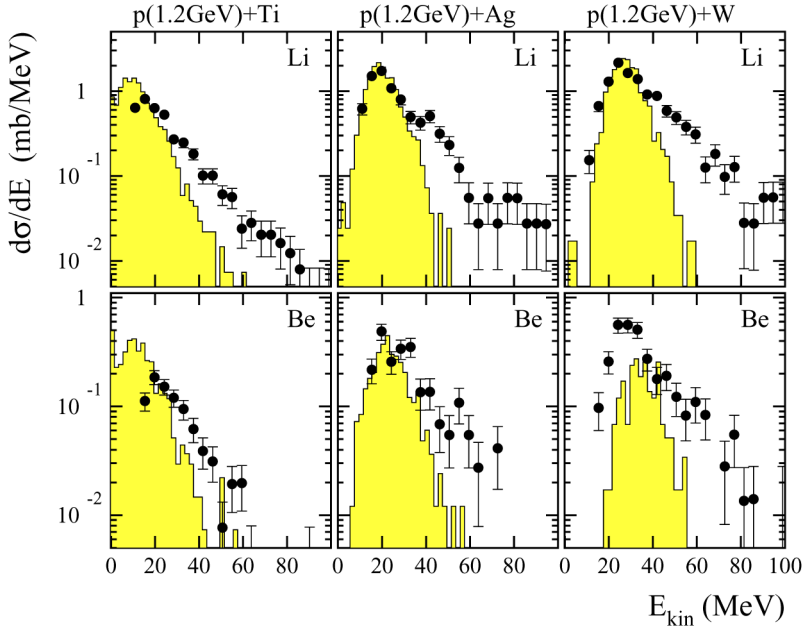


Fig. 18. Experimental (symbols) and calculated (shaded histograms) energy spectra of Li (top panels) and Be (lower panels) produced in the reactions 1.2 GeV p + Ti (left panels), p + Ag (middle panels) and p + W (right panels). The yields correspond to the integrals over 4π .

production cross sections in the overlapping region (see left panels of Fig. 18) gives some confidence to the applied corrections. In case of the heavy targets, the position of the peak simulated for the evaporation of Be is shifted to higher energies as compared to the measured data (see also the discussion further below). From the experimental energy distributions, however, it is obvious that the losses below threshold are negligible for heavier targets. The deduced corrections to the measured cross sections are substantial for light and medium-weight targets: for Li (Be) they amount to 140% (320%), 44% (98%), and 1% (8%) for targets of Al, Fe, and Ag.

The deduced total production cross sections for Li and Be isotopes, given for particle energies extrapolated to zero, are listed in Table 6. Contributions of 30% of the extrapolated yields are accounted for in the quoted total errors. A comparison of the present data with results from previous measurements and from simulation calculations is given in Figs. 19 and 20. The present ${}^9\text{Li}$ production cross sections agree within the experimental errors with results obtained in Ref. [84] at a somewhat lower bombarding energy of 1.0 GeV and targets between Al and U (Fig. 19). The present data for the long lived radionuclides ${}^7\text{Be}$ and ${}^{10}\text{Be}$ (Fig. 20) are confirmed by the cross sections obtained in activation measurements [25] for 1.2 GeV proton-induced reactions on targets between Al and Cu. Recent results have been reported for light fragment production cross sections measured in the reaction p + ${}^{56}\text{Fe}$ at 1 A GeV incident energy [85]. The results of a comparison with the present data for the reaction with ${}^{\text{nat}}\text{Fe}$ are inconsistent: while the data agree reasonably well for ${}^6\text{Li}$, ${}^7\text{Be}$, and ${}^9\text{Be}$, the cross section for the production of ${}^7\text{Li}$ is by a factor of about 4 smaller than the corresponding value obtained in this paper. The agreement with results of simulation calculations with INCL2 + GEMINI (see sections above), treating the evaporation of lithium and beryllium in the same way as for the hydrogen and helium isotopes, i.e., with a Hauser–Feshbach formalism, is quite well for the lighter Li and Be isotopes and the

Table 6

Production cross-sections σ_{tot} as measured in 1.2 GeV proton-induced spallation reactions for isotopes of Li and Be with kinetic energies of $0 \leq E \leq 100$ MeV

Target	${}^6\text{Li}$ (mb)	${}^7\text{Li}$ (mb)	${}^8\text{Li}$ (mb)	${}^9\text{Li}$ (mb)	${}^7\text{Be}$ (mb)	${}^9\text{Be}$ (mb)	${}^{10}\text{Be}$ (mb)
Al	9.1 ± 3.0	11.5 ± 3.8	1.7 ± 0.7	0.26 ± 0.17	7.8 ± 3.2	3.0 ± 1.4	2.8 ± 1.3
Ti	11.2 ± 2.6	14.4 ± 3.3	1.8 ± 0.5	0.24 ± 0.11	5.1 ± 1.6	2.3 ± 0.8	1.8 ± 0.7
Fe	9.9 ± 2.0	12.8 ± 2.5	1.6 ± 0.5	0.22 ± 0.13	5.1 ± 1.5	2.1 ± 0.7	1.0 ± 0.4
Ni	11.1 ± 1.8	12.4 ± 2.1	1.8 ± 0.5	0.18 ± 0.11	7.1 ± 1.8	2.0 ± 0.6	1.3 ± 0.5
Cu	10.6 ± 2.0	16.0 ± 2.9	1.5 ± 0.5	0.07 ± 0.08	4.9 ± 1.3	3.7 ± 1.1	1.6 ± 0.6
Zr	13.5 ± 1.9	16.0 ± 2.2	2.3 ± 0.7	0.60 ± 0.30	3.9 ± 0.7	2.0 ± 0.5	2.3 ± 0.6
Ag	15.1 ± 1.9	18.2 ± 2.2	2.6 ± 0.6	0.46 ± 0.22	4.2 ± 0.7	3.5 ± 0.8	3.1 ± 0.7
Ho	15.1 ± 1.9	27.4 ± 3.3	6.5 ± 1.2	1.55 ± 0.44	2.5 ± 0.4	6.7 ± 1.2	4.8 ± 0.9
Ta	15.3 ± 1.7	31.0 ± 3.2	5.1 ± 0.9	0.77 ± 0.26	3.4 ± 0.6	5.7 ± 1.0	5.7 ± 1.0
W	14.8 ± 1.7	28.8 ± 3.1	5.9 ± 1.1	1.22 ± 0.37	2.2 ± 0.4	5.7 ± 1.0	6.1 ± 1.1
Au	15.3 ± 1.6	31.5 ± 3.1	6.4 ± 1.0	1.47 ± 0.36	2.5 ± 0.4	6.1 ± 1.0	5.9 ± 1.0
Pb	11.9 ± 1.7	33.0 ± 4.1	6.7 ± 1.2	1.88 ± 0.54	2.0 ± 0.5	6.3 ± 1.2	6.3 ± 1.3
Th	16.9 ± 1.9	35.5 ± 3.5	10.1 ± 1.5	2.87 ± 0.71	2.0 ± 0.4	7.3 ± 1.2	10.4 ± 1.7

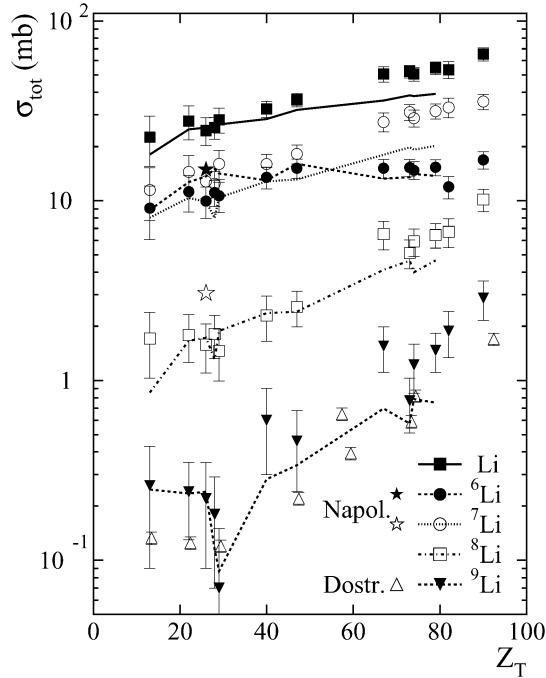


Fig. 19. Experimental (symbols) and calculated (lines) production cross sections of ${}^{6,7,8,9}\text{Li}$ with energies up to 100 MeV as a function of the target atomic number Z_T . The summed cross sections of all isotopes is also shown (Li). The data for ${}^6\text{Li}$ and ${}^7\text{Li}$ of Napolitani et al. [85] and results of Dostrovsky et al. [84] for ${}^9\text{Li}$ are plotted for comparison.

lighter targets. The calculations underestimate the experimental cross sections more significantly for heavier IMFs and heavier target nuclei. Discrepancies are larger for Be than for Li, and some trends are incorrectly predicted for Be branching ratios.

The underestimation of Li and Be production by INCL2 + GEMINI for heavier target nuclei may be attributed to the fact that the physics of statistical emission of complex IMFs from a heavy

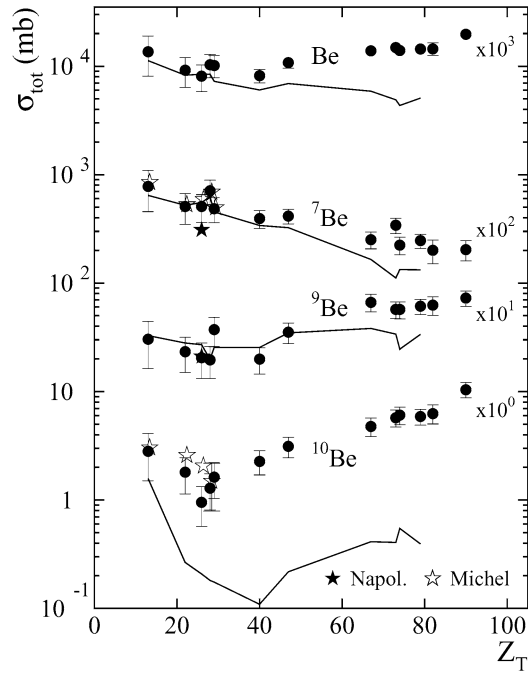


Fig. 20. Experimental (filled circles) and calculated (lines) production cross sections of $^{7,9,10}\text{Be}$ with energies up to 100 MeV as a function of the target atomic number Z_T . The summed cross sections of all isotopes is also shown (Be). For comparison the results of Michel et al. [25] for ^7Be and ^{10}Be and of Napolitani et al. [85] for ^7Be and ^9Be are indicated by open and solid stars, respectively.

nucleus is not well represented by a scenario of volume emission from the interior of such a nucleus at normal density. The corresponding Coulomb barriers for such processes are estimated to be 5–10 times larger than prevailing nuclear temperatures. Both the relatively large IMF yields and the measured energy spectra (see Fig. 18) are in qualitative support of a new statistical model [86] describing the emission of complex clusters from hot, expanded nuclei. In this model, the entropy associated with the enlarged surface of an expanded nucleus plays an important role in driving its binary or multiple cluster decay. Effective emission barriers in this model are naturally lower than actual barriers calculated for nuclei at their normal matter densities.

For lighter targets such as Al and Ti, it becomes conceptually more difficult to distinguish between evaporated IMFs and target residues. Here, an increasing portion of the detected lithium and, in particular, beryllium fragments is probably represented by evaporation residues of the original target nuclei, rather than IMFs having been evaporated during the de-excitation chain. Converting, as described in Section 3.2.2, the cross section into multiplicity, one observes that the multiplicity of Be from reactions on Al is about 3 times larger than for heavy targets. Nevertheless, absolute IMF multiplicities even for these lighter targets remain small; the mean multiplicity is about 0.03 for Li and 0.01 for Be. Consequently, the mean overall energy carried off per reaction by evaporated IMFs is also small, on average less than 2 MeV.

At high particle kinetic energies, the energy spectra of IMFs (Fig. 18) and LCPs (Fig. 7) show very similar exponential behaviour. In this domain, the experimental yields are considerably larger than those calculated for evaporated particles. Employing the same method as in the extraction of the PE component for the LCPs discussed in Section 3.2.2, one obtains PE contri-

butions to the respective total yields of about 25% for Li and about 15% for Be. These values are relatively independent of the target atomic number Z_T , except for the Al, where these contributions are smaller than 10%. For the Al-target, one may expect such low yields, if the IMFs are actually target-like residues (as discussed above). For heavy targets, however, the relative yield of the highly energetic IMF component is similar in magnitude to that obtained in Section 3.2.2 for the PE emission of ^4He -particles.

In the case of LCPs, a strong argument in favour of an identification of this high-energy component with PE emission was its larger forward/backward asymmetry compared to the low-energy evaporative component (see Fig. 12). In order to illustrate this characteristic signal for Li and Be fragments, in the left panels of Fig. 21 the energy spectra of these IMFs measured at a forward angle (30°) are compared with those detected at a more backward angle (150°). Despite the low statistical accuracy, a significant forward/backward yield asymmetry is observed. Energy thresholds (indicated by the dashed lines in Fig. 21) to distinguish approximately between low- and high-energy components have been set according to the calculated spectra of evaporated IMFs as shown in Fig. 18. The separated angular distributions of both components, shown in the

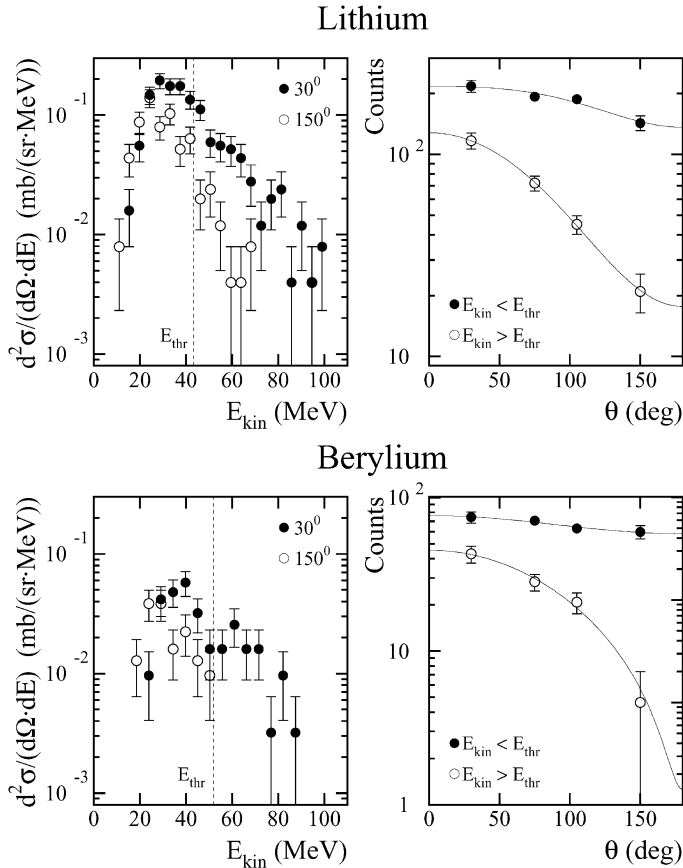


Fig. 21. Left panels: experimental energy spectra of Li (top panel) and Be (lower panel) at 30° (●) and 150° (○) from the reaction 1.2 GeV p + Au. Right panels: angular distributions of Li and Be with energies larger (○) and smaller (●) than the energy defined by the dashed line in the left panels at 42 MeV for Li and at 52 MeV for Be.

right panels of Fig. 21, demonstrate more quantitatively the difference between evaporative and PE emission.

The observed high forward/backward asymmetry for highly energetic IMFs rules out the hypothesis that these IMFs are evaporated from extremely high excited nuclei produced in processes in which a much larger fraction of the initial proton energy than predicted by the INCL2 code is converted to thermal excitation of the target nucleus. Indeed, one rather concludes that the highly energetic Li and Be fragments originate from a PE-process that is somewhat similar to that leading to the fast emission of energetic LCPs. However, the precise nature of such a PE emission process remains unclear. A coalescence model of formation and early emission of relatively heavy IMFs does not present a plausible scenario.

4. Conclusions

In the present work, systematics of total production cross sections are reported for hydrogen, helium, lithium, and beryllium isotopes emitted in 1.2 GeV proton-induced reactions on 13 targets between Al and Th. These isotope-resolved cross sections have been derived with typical total uncertainties of 8–15%, for LCPs, or 10–30%, for IMFs. In order to deduce total cross sections the measured particle energy spectra have been extrapolated below the experimental detection thresholds to zero energy. This procedure results in uncertainties with values depending on the target Coulomb barriers. The associated errors are larger for the lighter target elements with lower barriers, in particular for Al.

Due to the reasons discussed in Section 3.1 we consider the new data obtained in the present experiment for LCP production in 1.2 GeV proton-induced reactions as the final results of the NESSI Collaboration, thus replacing the corresponding data from earlier experiments published by Enke et al. [9].

Precisely measured shapes of particle energy spectra allow one to decompose the ${}^1,2,3\text{H}$ and ${}^{3,4}\text{He}$ production cross sections into evaporative and pre-equilibrium components. The deduced contributions of PE emission amount to 40–60% for ${}^2\text{H}$ and ${}^3\text{He}$, to 20–40% for ${}^3\text{H}$, and to only 5–20% for ${}^4\text{He}$ of the total emission. Very similar relative yields (15–25%) have been deduced for the PE emission of Li and Be fragments. The cross sections of evaporated particles are quantitatively reproduced by calculations based on a combination of the codes INCL2.0 and GEMINI. The PE emission of composite particles, however, is neglected in the models.

The experimentally obtained ratio between PE cross sections of deuterons and protons clearly scales with the neutron to mass number N_T/A_T of the target nucleus. This behaviour is in good agreement with the concept that deuterons are formed by the fusion of fast cascade nucleons with neutrons respectively protons at the nuclear surface, i.e., with the description by surface coalescence [12,59]. For tritons and ${}^3\text{He}$, the agreement between experimental data and similar estimates is not as perfect, but the coalescence approach seems to be an important mechanism also for these PE particles. The PE emission of ${}^4\text{He}$ and heavier clusters, however, is difficult to understand in the framework of a coalescence model, and other descriptions are needed to account for the observed yields. It is therefore of considerable interest to consider new formation and emission models for complex particles. The present systematic data, collected over a wide range of target nuclei, provide excellent testing grounds for this task.

The angular and energy distributions of non-evaporative protons are, in general, well described by the INCL2 calculations. At energies below 20 MeV the yield of protons is, however, overestimated by the INC calculations, whereas for neutrons no significant discrepancy was ob-

served [59]. It has been also noticed that the angular distributions of PE composite particles are very similar, and their dependence from the size of the target nucleus is not very pronounced.

The calculated mean excitation energy deposited by the initial intra-nuclear cascade—a prerequisite for any further statistical decay calculation—agrees in INCL2 simulations very well with the mean excitation energy deduced from the measured mean multiplicities of light charged particles and neutrons. This finding corroborates the previously observed agreement between calculated and experimentally deduced excitation energy distributions [9,12,13] for selected target nuclei. Most likely, PE composite particle emission does not significantly reduce the mean excitation energy of the target remnant. Rather, these PE emission processes induce a redistribution of energies between all energetic PE particles, i.e., nucleons, composite LCPs, as well as intermediate-mass clusters.

Additionally to the thermal excitation energy, the mean linear momentum, transferred during the prompt intra-nuclear cascade from the incident beam proton to the heavy residue, represents a further observable characterising nuclear excitation. In the present work, this independent observable was deduced from the anisotropy of the angular distributions of the evaporated ^4He particles and found to agree quite well with the INCL2 predictions corroborating the above results.

Acknowledgements

We are indebted to the COSY staff for the good beam quality, and to J. Cugnon and A. Boudard for providing us with the codes INCL2.0, INCL4.2, and KHSv3p. For their reliable technical support before or during the data taking runs, we thank, in particular, K. Nünighoff, N. Paul, K. Pysz, H. Schaal, G. Sterzenbach, and M. Wohlmuther. This work was partially supported by the EU-TMR project ERBFMRXCT980244 and by US-DOE Grant No. DE-FG02-88ER40414.

References

- [1] G.S. Bauer, Nucl. Instrum. Methods A 463 (2001) 505.
- [2] H. Nifenecker, et al., Nucl. Instrum. Methods A 463 (2001) 428.
- [3] High Energy Astrophysics, vols. 1 and 2, Cambridge Univ. Press, Cambridge, 1997.
- [4] T.K. Gaiser, Cosmic Rays and Particles Physics, Cambridge Univ. Press, Cambridge, 1992.
- [5] R. Michel, I. Leya, L. Borges, Nucl. Instrum. Methods B 113 (1996) 434.
- [6] R.C. Reedy, J.R. Arnold, J. Geophys. Res. 77 (1972) 537.
- [7] L. Pienkowski, et al., Phys. Rev. C 56 (1997) 1909.
- [8] D. Hilscher, et al., Nucl. Instrum. Methods A 414 (1998) 100.
- [9] M. Enke, et al., Nucl. Phys. A 657 (1999) 317.
- [10] A. Letourneau, et al., Nucl. Instrum. Methods B 170 (2000) 299.
- [11] C.-M. Herbach, et al., in: D. Filges, F. Goldenbaum, Y. Yariv (Eds.), Proceedings of the Fifth Workshop on Simulating Accelerator Radiation Environments, 17–18 July 2000, OECD Headquarters, Paris, ESS 112-01-T, p. 7.
- [12] A. Letourneau, et al., Nucl. Phys. A 712 (2002) 133.
- [13] D. Hilscher, et al., in: A.C. Mueller, M. Mirea, L. Tassan-Got (Eds.), Proceedings of the International Workshop on the New Applications of Nuclear Fission, 7–12 September 2003, Bucharest, Romania, World Scientific, Singapore, 2004, p. 75.
- [14] F. Goldenbaum, et al., Phys. Rev. Lett. 77 (1996) 1230.
- [15] C.-M. Herbach, et al., in: A. Kelic, K.-H. Schmidt (Eds.), Proceedings of the Workshop on Nuclear Data for the Transmutation of Nuclear Waste, September 2003, GSI Darmstadt, <http://www-wnt.gsi.de/tramu/>.
- [16] U. Jahnke, et al., Phys. Rev. Lett. 83 (1999) 4959.
- [17] B. Lott, et al., Phys. Rev. C 63 (2001) 034616.
- [18] O.A. Schaeffer, J. Zähringer, Phys. Rev. 113 (1959) 674.
- [19] R.H. Bieri, W. Rutsch, Helv. Phys. Acta 35 (1962) 553.

- [20] K. Goebel, H. Schultes, J. Zähringer, Report CERN 64-12, 1964.
- [21] J.B. Cumming, et al., Phys. Rev. C 10 (1974) 739.
- [22] S.L. Green, et al., J. Nucl. Mater. 155–157 (1988) 1350.
- [23] R. Michel, et al., Nucl. Instrum. Methods B 42 (1989) 76.
- [24] M. Noguchi, et al., Appl. Radiat. Isot. 42 (1991) 577.
- [25] R. Michel, et al., Nucl. Instrum. Methods B 103 (1995) 183.
- [26] I. Leya, et al., Nucl. Instrum. Methods B 145 (1998) 449.
- [27] I. Leya, et al., Nucl. Instrum. Methods B 229 (2005) 1.
- [28] E.K. Hyde, G.W. Butler, A.M. Poskanzer, Phys. Rev. C 4 (1971) 1759.
- [29] A.M. Poskanzer, G.W. Butler, E.K. Hyde, Phys. Rev. C 3 (1971) 882.
- [30] E.M. Volnin, et al., Phys. Lett. B 55 (1975) 409.
- [31] G.D. Westfall, et al., Phys. Rev. C 17 (1978) 1368.
- [32] R.E.L. Green, R.G. Korteling, Phys. Rev. C 22 (1980) 1594.
- [33] L.N. Andronenko, et al., NPI Preprint, Gatchina, Russia, NP-38-1980, 1994.
- [34] D.L. Olson, et al., Phys. Rev. 28 (1983) 1602.
- [35] A. Korejwo, et al., J. Phys. G: Nucl. Part. Phys. 26 (2000) 1171.
- [36] A. Korejwo, et al., J. Phys. G: Nucl. Part. Phys. 28 (2002) 1199.
- [37] K.K. Gudima, S.G. Mashnik, V.D. Toneev, Nucl. Phys. A 401 (1983) 329.
- [38] S.G. Mashnik, A.J. Sierk, K. Gudima, nucl-th/0208048.
- [39] R.E. Prael, H. Lichtenstein, LANL Report, Los Alamos, LA-UR-89-3014, 1989.
- [40] R.E. Prael, M. Bozoian, LANL Report, Los Alamos, LA-UR-88-3238, 1988.
- [41] A. Fassó, et al., in: Proceedings of CHEP03 Computing of High Energy and Nuclear Physics, March 2003, La Jolla, USA, hep-ph/0306267.
- [42] J.J. Griffin, Phys. Rev. Lett. 17 (1966) 478.
- [43] M. Blann, Phys. Rev. Lett. 27 (1971) 337.
- [44] P.E. Hodgson, E. Béták, Phys. Rep. 374 (2003) 1.
- [45] A. Chevarier, et al., Phys. Rev. C 11 (1975) 886.
- [46] C.K. Cline, Nucl. Phys. A 193 (1972) 417.
- [47] A. Iwamoto, K. Harada, Phys. Rev. C 26 (1982) 1821.
- [48] R.E.L. Green, R.G. Korteling, Phys. Rev. C 18 (1978) 311.
- [49] S. Das Gupta, A.Z. Mekjian, Phys. Rep. 72 (1981) 131.
- [50] G.F. Bertsch, S. Das Gupta, Phys. Rep. 160 (1988) 189.
- [51] D.H. Boal, J.H. Reid, Phys. Rev. C 29 (1984) 973.
- [52] D.H. Boal, Adv. Nucl. Phys. 15 (1985) 85.
- [53] R. Hagedorn, Phys. Rev. Lett. 5 (1960) 276.
- [54] D.B. Barlow, Phys. Rev. C 45 (1992) 293.
- [55] S. Nagamiya, M. Gyulassy, Adv. Nucl. Phys. 13 (1984) 201.
- [56] E.Y. Golubeva, private communication, 2000.
- [57] S.T. Buttler, C.A. Pearson, Phys. Rev. 129 (1963) 836.
- [58] A. Schwarzschild, C. Župančič, Phys. Rev. 129 (1963) 854.
- [59] A. Boudard, et al., Nucl. Phys. A 740 (2004) 195.
- [60] J. Franz, et al., Nucl. Phys. A 510 (1990) 774.
- [61] S. Chiba, et al., Phys. Rev. C 54 (1996) 285.
- [62] S. Fan, Z. Li, Z. Zhao, Nucl. Sci. Eng. 142 (2002) 195.
- [63] S. Fan, et al., Nucl. Sci. Eng. 144 (2003) 219.
- [64] J. Cugnon, C. Volant, S. Vuillier, Nucl. Phys. A 620 (1997) 475.
- [65] R.J. Charity, et al., Nucl. Phys. A 483 (1988) 371, GEMINI-code obtained from <http://wunmr.wustl.edu>.
- [66] H.P. Wellisch, D. Axen, Phys. Rev. C 54 (1996) 1329, revised by R.E. Prael, M.B. Chadwick, LANL Report, Los Alamos, LA-UR-97-1745, 1989.
- [67] A. Boudard, et al., Phys. Rev. C 66 (2002) 044615.
- [68] J.-J. Gaimard, K.-H. Schmidt, Nucl. Phys. A 531 (1991) 709.
- [69] A.R. Junghans, et al., Nucl. Phys. A 629 (1998) 635.
- [70] H.W. Bertini, Phys. Rev. A 131 (1963) 1801.
- [71] L. Dresner, ORNL Report, Oak Ridge, ORNL/TM-196, 1962.
- [72] O. Bersillon, Report CEA-N-2227, NEANDC (France) 220“L”, INDC(E) 49/L, 1981.
- [73] D. Filges, et al., Eur. Phys. J. A 11 (2001) 467.

- [74] A. Gilbert, et al., *Can. J. Phys.* 43 (1965) 1446.
- [75] U. Jahnke, et al., *Nucl. Instrum. Methods A* 508 (2003) 295.
- [76] C.-M. Herbach, et al., *Nucl. Instrum. Methods A* 508 (2003) 315.
- [77] J.P. Biersack, L.G. Haggmark, *Nucl. Instrum. Methods* 174 (1980) 257.
- [78] J.F. Ziegler, *J. Appl. Phys. (Rev. Appl. Phys.)* 85 (1999) 1249, see also SRIM2003, <http://www.srim.org>.
- [79] H.S. Virk, G.S. Randhawa, *Mater. Sci. Forum* 248–249 (1997) 33.
- [80] D. Hilscher, et al., *J. Nucl. Mater.* 296 (2001) 83.
- [81] C.-M. Herbach, et al., to be published.
- [82] C.-M. Herbach, et al., *Annual Report 2001*, FZ Jülich, Jül-3978, 2002, p. 207.
- [83] V.E. Viola, *Nucl. Phys. A* 502 (1989) 531c.
- [84] I. Dostrovsky, et al., *Phys. Rev. B* 139 (1965) 1513.
- [85] P. Napolitani, et al., *Phys. Rev. C* 70 (2004) 054607.
- [86] J. Toke, J. Lu, W.U. Schröder, *Phys. Rev. C* 67 (2003) 034609.